Heterogeneous microstructure development in additive friction-stir deposited Al-Mg-Si alloy

Peter C. Metz [a],[*],[1], Cole Franz [a],[1], Joshua Kincaid [b], Tony Schmitz [b],[c], Eric A. Lass [a], Sudarsanam S. Babu [b],[c], Katharine Page [a],[d],[*]

[a] Department of Materials Science and Engineering, University of Tennessee, Knoxville, TN 37996, USA
[b] Department of Mechanical, Aerospace, and Biomedical Engineering, University of Tennessee, Knoxville, TN 37996, USA
[c] Manufacturing Sciences Division, Oak Ridge National Laboratory, Knoxville, TN, 37932, USA
[d] Neutron Scattering Division, Oak Ridge National Laboratory, Oak Ridge, TN 37831, USA

ARTICLE INFO

ABSTRACT

Aluminum alloy 6061-T6511 was printed by additive friction stir deposition onto a cast aluminum A206-T4 plate. Metallography, X-ray powder diffraction, X-ray pole figure analysis, and electron backscatter diffraction of the center, advancing side, and retreating side of the 6061 deposit reveals different texture and grain structure characteristics across the transverse direction and through each layer. These distinct microstructural domains are indicative of spatially varied temperature, strain rate, and strain accumulation during deposition, and consequently of regions differing in the fraction of dynamic recovery and dynamic recrystallization during deposition. Hardness mapping over the complete cross section at 0.75 mm resolution shows the alloy continues to age after active deposition, and hardness increases over the 5 mm nearest the final printed layer. Additional mapping at 0.10 mm resolution shows intralayer hardness variations of the deposit on the retreating side. These observations demonstrate that complex and non-uniform thermal-mechanical transients occur during additive friction stir deposition, resulting in spatially non-uniform microstructure and properties.

1. Introduction

Fusion-based metal additive manufacturing (AM) processes constitute complex melting, solidification, and solid-state transformations in response to complex thermomechanical transients. Consequently, some alloys that are prone to cracking during solidification are not appropriate for fusion-based AM. Solid-state additive friction stir deposition (AFSD) overcomes this challenge by joining metallic feedstocks without melting [1–6]. While metal additive manufacturing by AFSD has many attractive attributes, the technique is new compared with traditional AM methods. Consequently, a robust understanding of process-structure-property (PSP) relationships is still evolving. Specifically, understanding the correlation between the machine inputs and the state of material feedstocks to microstructural gradients,[7,8] hardness variations, [9] scatter in strength, [10–12] fatigue, [9,10,13] and other material properties such as corrosion resistance [14] is critical to the widespread adoption of the AFSD technology.

Microstructure and texture development in aluminum alloys during

hot deformation has been extensively studied [15]. As with other elevated temperature severe plastic deformation (SPD) methods, microstructure development proceeds through several activated processes broadly grouped as recovery, recrystallization, and grain growth, and further distinguished by whether they proceed concurrently with (dynamically) or subsequent to (statically) deformation [16,17]. Importantly, these microscopic deformation mechanisms strongly depend on alloy composition and the thermal-mechanical state during processing. Grain refinement during SPD is generally attributed to continuous dynamic recrystallization (cDRX). Further, grains in polycrystalline aggregates may undergo both rigid body and shear deformation during plastic deformation. As a result, the stability of particular crystallite orientations with reference to the applied deformation vector results in texture development [18]. Different deformation sequences, thermomechanical parameters, and their relative orientations with reference to sample coordinates impose different velocity gradients and strain rates on the material systems. Therefore, in general, care must be taken in comparing final textures within a finished product [19]. For

---

* Corresponding authors at: Department of Materials Science and Engineering, University of Tennessee, Knoxville, TN 37996, USA.
E-mail addresses: pmetz1@utk.edu (P.C. Metz), kpage10@utk.edu (K. Page).
[1] These authors contributed equally.

example, Beyerlein and Tóth have observed similarities in texture developed during torsion and equal channel angular extrusion (ECAE). This result has been used as experimental validation of theory that predicts simple shear deformation in face-centered cubic (FCC) polycrystals. [19–22] The tacit assumption is that plastic deformation during AFSD or friction stir welding (FSW) resembles hot torsion testing and that one may expect shear textures in the final builds. This assumption is made based on many reports investigating shear deformation textures in ECAE, [19,20,22–27] hot torsion, [28–30] friction stir welding (FSW), [31–33] and other less common methods such as high-pressure torsion compaction. [34] Given the variety of boundary conditions imposed during AFSD (*e.g.,* Mason *et al.* [11]), this assumption may not hold in all situations, and the equivalence of AFSD and hot torsion has not been rigorously evaluated.

Predictive modeling of material characteristics including crystallographic texture as a function of spatial and temporal variation of thermal-mechanical conditions during any forming operation is of great interest to describe the formability and the properties of the final part. A large body of work on computational predictions of texture development exists, including Canova, [28] Montheillet, [29,30] and Toth, [18,35] among others, [36] enabling predictions of bulk properties in polycrystalline materials. [37] More recently, increased computational power has enabled calculation of spatially and temporally resolved thermal-mechanical conditions during FSW [38] and AFSD. [39–42] This may offer insights into the microstructure evolution in age hardening aluminum alloys, including dissolution of existing precipitates, homogenization of alloying elements, re-precipitation of hardening phases within matrix, work hardening, recrystallization, and grain boundary precipitation. Further, many characteristics of AFSD key to interpreting resulting microstructures and properties are impossible to observe *in situ* (*i.e.,* temperature, strain, strain rate, and flow stress) and therefore modeling is an invaluable tool. Recent modeling efforts have provided detailed predictions regarding the temperature, strain, and strain rate distributions and material trajectories beneath the AFSD tool [39–42]. However, these results have not been validated with comprehensive microstructure investigations.

Experimentally, microstructure development in AFSD [7,8,12, 43–46] and associated PSP correlations [9–11,46,47] has been reported in few cases. For example, Griffiths et al. [45] investigated microstructure development near the center of the deposit track in aluminum 6061 and in copper printed by AFSD. They report variation in crystallographic shear texture depending upon the rotation rate (Ω, rpm), travel velocity (V, mm/s), and the ratio of tool rotation to travel velocity (Ω/V, rotations/mm). However, this and similar studies have often focused on small regions of interest, often near the center of the deposit. Others have looked more broadly at interface characteristics identifying transverse asymmetry in the baseplate interface and a rapidly evolving microstructure where the feedstock impinges upon the deposit, [7,8] and identifying localized grain size refinement in the overlap region of parallel tracks. [46] Mason et al. [11] utilized crossed deposition tracks to produce Al 7050 with distinctive boundary conditions (*i.e.,* tool dwell, steady state, and path intersection) and performed electron backscatter diffraction (EBSD) characterization at different locations along the build direction, finding different grain size distributions and textures associated with the different thermal-mechanical histories. These regions were also associated with significantly different ultimate tensile strengths and elongations at failure. In summary, differences in the scope of material investigated have led authors to different conclusions about the uniformity of AFSD materials.

Finally, the thermomechanical transients experienced by the deposit influence the phase constituents and their distribution in the as-deposited microstructure. In precipitation hardening 6061, strengthening is achieved by precipitation of Mg_2Si precipitates from solid solution. This transformation follows a complex pathway marked by the formation of various metastable intermediates [48]. Peak hardness in AA6061 is typically associated with one of the metastable nanoscale

intermediates (β'' Mg_2Si), which may coexist with larger equilibrium β Mg_2Si particles. Typically, phase fractions are controlled by post-process heat treatment, including a high-temperature (T > = 80% T_m) solutionizing anneal, quench, and low-temperature aging (T *ca.* 25% T_m). In AFSD, Zhu et al. [49] demonstrated that strain-relieved aluminum lattice constant and the measured hardness vary over the build height, decreasing from the last-deposited layer through 10 mm of depth where these two quantities became invariant, suggesting 6061 is overaged in multilayer deposits. Further, the presence of fine secondary phases may facilitate recrystallization (*i.e.,* particle stimulated nucleation) and influence grain growth. In summary, microstructure development during AFSD of aluminum alloys has a complex relationship with precipitation, dissolution, dispersion, and fragmentation of any secondary phases within the matrix.

We have deposited widely used 6061 [50]. extruded bar by AFSD onto the common automotive casting alloy A206,[51] initially conceived as a repair application. This research focuses on metallographic, X-ray diffraction, and EBSD observations spanning a 3.5 cm x 3.2 cm cross section of AFSD 6061 in the transverse and normal direction plane. Microstructure variations were observed through the layer thickness (2.54 mm) and across the transverse direction of the deposit. On the retreating side, EBSD analysis spanning 3 mm of build height was performed to understand the variations in thermal-mechanical histories as a function of intralayer height. The resulting influence on mechanical heterogeneity was quantified using microhardness maps.

2. Materials and methods

2.1. Additive friction stir deposition

Aluminum alloy 6061 (assay: Al-0.91% Mg, 0.67% Si, 0.29% Fe, 0.18% Cu, 0.08% Mn, 0.05% Cr, 0.04% Zn, 0.02% Ti wt%) feedstock was obtained in 9.5 mm (3/8 in) square bar stock in a T6 condition. Cast aluminum alloy A206 (typical: 4.6% Cu, 0.35% Mn, 0.25% Mg, 0.22% Ti) was obtained for the base plate as 38 mm (1.5 in) thick plate in a T4 condition. AFSD was performed with an L3 machine (MELD Manufacturing Corp., USA) using a featured tool with 4 protrusions; the deposition details are summarized in Table 1. The print entailed two one-directional paths about 250 mm in length, 50 mm in width, and separated by 50 mm. The first layer height was 1.25 mm (0.050 in), and subsequent layer height was 2.54 mm (0.100 in). After deposition of all layers, the two tracks were milled to remove flash (about 9 mm around the periphery) and surface roughness. The two print tracks were separated, and a 10 mm thick slice was extracted from the traveling region of the right-side deposit away from the starting and stopping zones using wire electrical discharge machining (EDM). The deposit and section

Table 1
Process details.

Materials			
	Alloy	Temper	† Hardness
Baseplate	A206	T4	120 HV (110 HB)
Feedstock	6061	T6511	111 HV (95 HB)
Process Parameters			
Spindle Speed (Ω)	5.00 s^{-1} (300 rpm)		
Travel Rate (V)	1.80 mm·s^{-1} (4.25 in·min^{-1})		
Feed Rate (F)	2.54 mm·s^{-1} (6.00 in·min^{-1})		
Pitch (Ω/V)	2.78 mm^{-1} (70.6 in^{-1})		
*Spindle Torque	271 N·m (200 lbf·ft)		
*Extrusion Force	6700-8900 N (1500 – 2000 lbf)		
Layer Height	2.54 mm (0.100 in)		
Layer Height, initial	1.27 mm (0.050 in)		
Layer count	10		
Tool nub	0.635 mm (0.025 in)		
Tool lubricant	graphite		

* Dependent parameters.

† Typical values [50,51] converted by ASTM E14-12b.

studied in this work are shown in Fig. 1. The characteristic directions of the deposit in the orthonormal reference frame are denoted as the transverse direction (TD ∥ x), the longitudinal direction (LD ∥ y), and the normal direction (ND ∥ x), forming a right-handed coordinate system (Fig. 1a). The right-handed tool rotation vector is colinear with ND.

2.2. Metallography

Samples were polished using standard abrasives, concluding with a 0.05 μm diamond suspension. The microstructure was revealed through a two-step etching process. First, the grain boundaries were etched. Samples were iteratively immersed for 30 s in 1 wt% (0.25 M) aqueous NaOH and washed with DI water six times. Second, a color etchant was applied to differentiate grain characteristics. Samples were immersed in Weck's reagent (4 g KMnO$_4$, 1 g NaOH, 100 mL DI H$_2$O) for 20 s, then rinsed in methanol. Optical microscopy was performed using a Keyence VHX 7000 and composite images were stitched with the software package Image Composite Editor (ICE, Microsoft).

2.3. Microhardness

Microhardness mapping was performed on a LECO Microhardness AMH55 automatic indentation system equipped with a Vickers indenter of 40 μm mean diagonal length (d$_l$). The full area (Fig. 3) was mapped with a 750 μm x 750 μm grid (41 columns by 42 rows) with a 100 gf indentation load and 13 s dwell time. The area overlapping the retreating zone EBSD ROI (Fig. 3) was mapped with a 100 μm x 100 μm grid (12 columns by 30 rows), with a 50 gf indentation load and 13 s dwell time. The indent spacing was in both cases at least 2.5 times the d$_l$ in accordance with ASTM E384–22.

2.4. X-ray powder diffraction

X-ray powder diffraction (PXRD) data was collected using a Panalytical Empyrean diffractometer equipped with a 240 mm goniometer and translational stage for sample positioning. A line-focus copper X-ray tube was used with a 0.04 rad Soller slit, programmable divergence slit, and beam mask to illuminate a fixed sample area (*ca.* 4.5 mm ∥ TD, 20 mm ∥ ND). The diffracted beam path included a 0.04 rad Soller slit, nickel filter, and PIXcel^{3D} position sensitive detector. Data were analyzed using the software package TOPAS. [52].

The resulting PXRD data were analyzed using the software package TOPAS. [52] The instrument resolution was modeled using the fundamental parameters approach, [53] and was optimized for the instrumental configuration in this work using NIST SRM 640 f (Si). Preferred orientation was modeled using an 8th order spherical harmonic. [54] Microstructural line broadening was modeled using the TOPAS

implementation of whole powder pattern modeling (WPPM); [55] size broadening was represented assuming a log-normal spherical crystallite size distribution, and anisotropic strain broadening was represented using the empirical Popa-Adler-Houska (PAH) model. [56] Additional details on these models are included in Appendix 4.

2.5. X-ray pole figure analysis

X-ray pole figures were collected using a Panalytical X'Pert3 MRD diffractometer equipped with a 320 mm goniometer and Eulerian cradle for sample positioning. A point-focus copper X-ray tube was used in conjunction with double crossed slits to control sample illumination, while the diffracted beam path comprised a 0.27° parallel plate collimator and xenon proportional detector. φ-circles were collected for inclinations $0 < \chi < 75°$ with 5° increments of φ and χ at the 111, 200, 220, and 311 Bragg positions. The crossed slits for each Bragg position were selected so that the area illuminated by the beam remained near 5 mm x 5 mm. Data correction, orientation distribution function (ODF) reconstruction, and pole figure analysis was performed using the software package MTEX. [57,58].

Shear deformation textures in FCC metals are often presented in context of their 111 pole figure (Fig. 2a) or, using the Bunge convention for Euler angles, [59] the 45° φ$_2$ ODF slice (Fig. 2b). These data represent the orientation distribution of the observed polycrystal, which for SPD processes like ECAE, torsion, and AFSD are often found to collect along two key fibers (A, B) and a handful of ideal orientations along those fibers (A*, A, B, C) These fibers and ideal orientations align particular crystallite orientations with the deformation, and so the resulting texture influences the ratio between the applied flow stress and the critically resolved shear stress responsible for dislocation motion (*i.e.,* the Taylor factor, M). [60] These details are collected in Table 2.

The first step in the analysis of component textures in AFSD materials is determining the orientation of the local deformation reference frame defined by a shear direction vector (SD) and a shear plane normal vector (SPN). In ECAE and torsion, these directions are well defined with respect to the machine or sample reference frame. Because the plastic flow induced during AFSD is not rigidly constrained, and hence not known *a priori,* the textures observed in the TD-ND-LD sample reference frame are not immediately interpretable from reported shear deformation textures. This is analogous to the observation of texture rotation in FSW. [33] In this work, we determined the rotation between the TD-ND observation plane and the local deformation reference frame by least-squares minimization of the difference between a proposed model texture and the rotated observed texture. These analyses were performed using MTEX and the MATLAB Optimization Toolbox. Additional discussion of the method is given in Appendix 2.
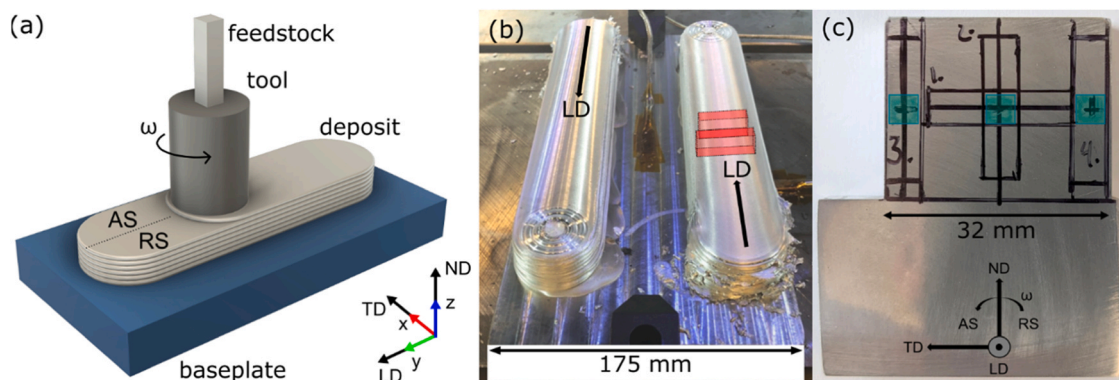

Fig. 1. A schematic rendering of the AFSD process and the characteristic directions discussed in this work (a), a view of the deposit with longitudinal direction (→) and approximate section location (orange region) annotated (b), and the TD-ND cross section studied in this work (c). PXRD data were measured in the enumerated oblong rectangles (*ca.* 4.5 mm × 20 mm), and pole figures were measured at the locations indicated by green squares (*ca.* 5 mm x 5 mm).
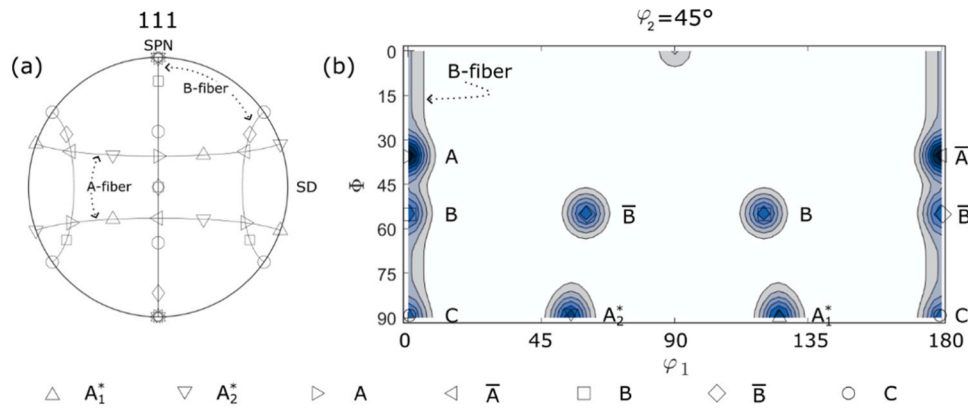
Fig. 2. Ideal shear deformation textures (markers) and fiber textures (lines) observed for ECAE and hot torsion of FCC metals: 111 pole figure (a), and 45° φ₂ ODF section (b).

Table 2
Ideal shear textures in FCC metals with corresponding Taylor factors, after Toth. [18].

A-fiber	B-fiber	SPN {hkl}	SD <uvw>	Taylor factor
A	A	$(11\bar{1})$	$[1\bar{1}0]$	1
A_1^*		$(11\bar{1})$	$[2\bar{1}1]$	$2/\sqrt{3}$
$\bar{A}$		$(11\bar{1})$	$[1\bar{1}0]$	1
A_2^*		$(11\bar{1})$	$[101]$	$2/\sqrt{3}$
	B	$(11\bar{1})$	$[1\bar{1}0]$	$\sqrt{2}$
	C	(001)	$[1\bar{1}0]$	$\sqrt{3}$
	$\bar{B}$	$(\bar{1}\bar{1}2)$	$[1\bar{1}0]$	$\sqrt{2}$

2.6. Electron backscatter diffraction

Regions of interest were extracted using wire EDM. Sample preparation for EBSD followed the same polishing procedure described previously. Afterwards, samples were vibratory polished for 2 h using 0.02 µm colloidal silica. The retreating side sample was ion milled for 20 min at an angle of 10° under 5 kV accelerating voltage and 1.5 kV discharge voltage, immediately transferred to a ZEISS Crossbeam 550 SEM equipped with an OXFORD Symmetry detector, and EBSD patterns were collected with 0.4 µm step size. Large-area mapping and data stitching was performed using the AZtecHKL software (Oxford Instruments); 10% scan overlap was employed. The advancing side and central region samples were transferred immediately after vibratory polishing to a HELIOS 5 Hydra DualBeam SEM (Thermo Fischer Scientific) equipped with an EDAX Velocity EBSD detector, and EBSD patterns were collected with 0.9 µm and 0.4 µm step size. These step sizes are in accordance with ISO 13067:2020, which suggests step size should be less than 10% of the average grain size [61,62]. All measurements were performed using a 25 keV electron beam and 20 nA beam current. Post-processing of EBSD data was performed in MATLAB using the MTEX toolbox. [57] ODF reconstruction was performed using kernel density estimation [63] employing a de la Vallée Poussin kernel with 5° halfwidth [64]. Grain reconstruction using a 10° misorientation [65] followed denoising using a half-quadratic filter [66] with regularization parameter α = 0.5; grains with 3 or fewer pixels were rejected.

3. Results and discussion

3.1. Metallography

The sample cross section is presented in Fig. 3 and magnified regions of interest are presented in Fig. 4. Fig. 3 is centered on the deposit track, and the left- and right-hand sides of the micrograph depict the advancing and retreating sides, respectively. The local color contrast can
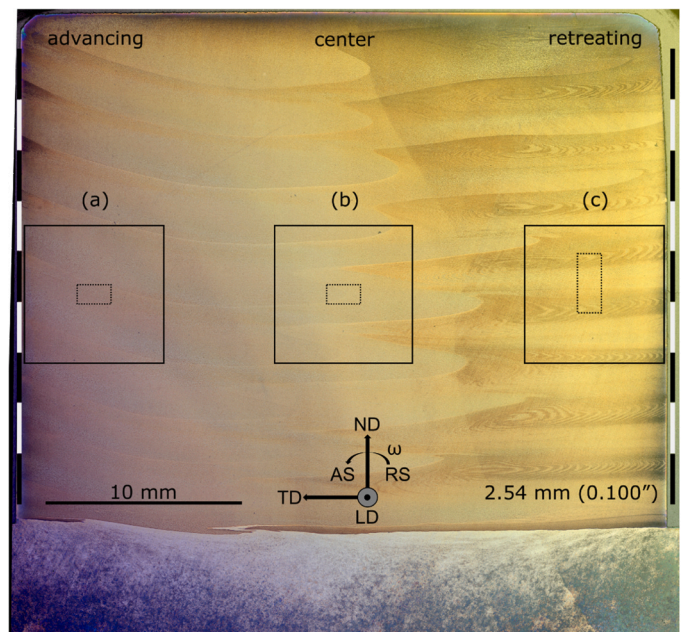

Fig. 3. Optical metallography of a polished and etched TD-ND cross section clearly reveals distinct microstructural domains. Pole figures were collected in the vicinity of (a-c); higher magnification images of these regions are presented in Fig. 4. EBSD was measured in the smaller inset regions (dotted lines).

be interpreted as differences in crystallite morphology and texture produced by variable thickness of epitaxial film produced by Weck's etchant [67,68].

The microstructure in this TD-ND cross section integrates the total accumulated deformation during repeated passage of the AFSD tool, revealing layers that correspond roughly to the target layer height (2.54 mm or 0.100 in). Repetition of distinctive microstructure features from layer to layer implies that the thermal-mechanical processing conditions are fairly repeatable. The advancing side shows a subtle pattern of lighter larger apparent grains, smaller darker apparent grains, and bright thin lines that repeat at *ca.* 2.5 mm intervals (Fig. 4a). The retreating side shows alternating bright and dark regions that are more complex (Fig. 4c) but repeat with similar *ca.* 2.5 mm intervals. Upon close inspection, the brighter regions are seen to comprise thin striations spaced on the order of 10^1 µm apart and inclined *ca.* 9° from the TD (Fig. 4 f), while and darker regions comprise curved bands of alternating large and small grain size spaced on the order of 10^2 µm apart (Fig. 4c). The centerline shows a mixing of these two microstructures where
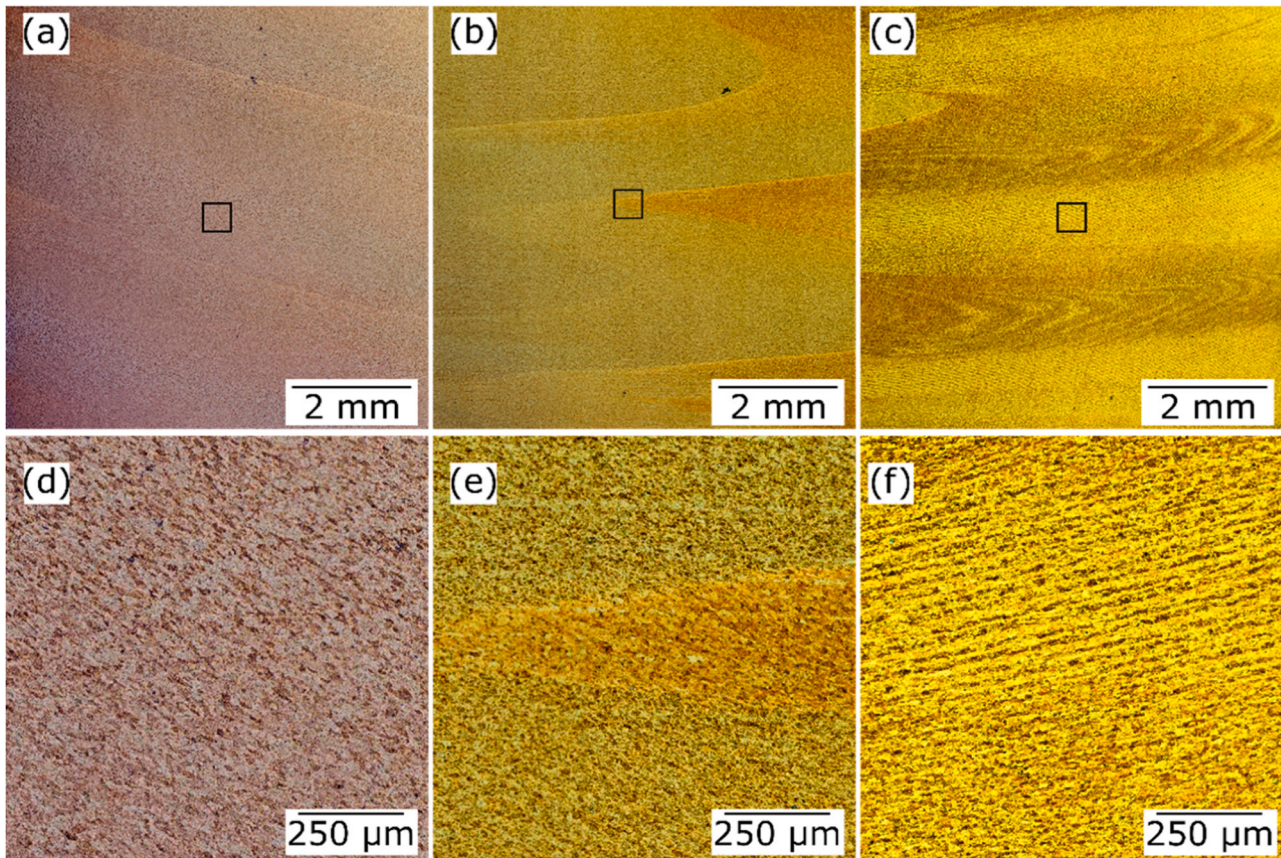
Fig. 4. Polished and tint-etched micrographs corresponding to regions (a-c) in Fig. 3 and magnified regions (d-f, corresponding with inset in a-c). Panel-to-panel variations in apparent color are an artifact of sample preparation. Local variations in apparent color are caused by microstructure differences.

material is drawn from AS to RS (-TD) on the front side of the AFSD tool and from RS to AS (+TD) on the back side (Fig. 4b). The extent to which the advancing side microstructure impinges on the retreating side varies from layer to layer, perhaps indicating some irreproducibility from layer to layer, or else some subtle variation in the accumulated strain along the longitudinal direction.

The differences in microstructure among the central, advancing, and retreating regions are rationalized by deformation within specific strain-rate and temperature regimes. During the deposition process, material is compressed between the substrate and tool shoulder. As a result, material flows away from the rotation axis *via* squeeze flow, [69] and the magnitude of squeeze flow differs on the advancing and retreating sides, as evidenced by tracer flow experiments from FSW [70] and AFSD [7]. These studies demonstrate that the shear strain rate ($\dot{\varepsilon}$) is highest in the advancing side and lowest in the retreating side. Further, thermoplastic deformation can occur either uniformly or from localized slip depending on the interaction of strain rate and temperature, where macroscopic shear band formation is characteristic of flow localization. [71–73] The coarse banded microstructure observed on the retreating side resembles onion rings commonly observed in FSW [74] or the hooked features observed in squeeze flow or barreling, [69,75] though the origin here is unclear. Optical investigation of the alternating bands demonstrates a bimodal grain size, where the light and dark bands each have consistent grain size differences relative to one another (Fig. 3 f), reinforcing the idea of flow localization [76]. In a process map developed by Sarkar *et al.* [72] for a similar Al-Mg-Si alloy, such flow localization was identified for the hot deformation at T = 300–350 °C and $\dot{\varepsilon}$ = 0.5–1.0 s^{-1}. Similarly, Duckham et al. [71] identified the prevalence of shear band formation at T < 350 °C and $\dot{\varepsilon}$ = 1 s^{-1}, or more specifically for the range of Zener-Hollomon parameter (Z, Appendix 1) between 9.2×10^{13} s^{-1} and 1.0×10^{14} s^{-1}. Thus, intralayer variation of the

observed microstructure features along both the TD and ND directions supports an inference of spatially heterogeneous thermomechanical process conditions.

3.2. Microhardness

The observed microhardness map for the AFSD deposit and 5 mm of baseplate is presented in Fig. 5a with projected statistics computed along the TD and ND directions. A 2.54 mm rule is annotated along the ND as a reference for the expected layer interface locations. The A206 substrate below the AFSD 6061 is relatively hard, approaching 100 HV within 1 mm of the AFSD interface. The AFSD 6061 deposit is uniform across all but the last couple deposited layers, with values near 45.7 ± 1.2 HV (mean ± 1 standard deviation). The hardness near the upper surface exhibits bowed contours that closely resemble the non-planar interface apparent in Fig. 3, with the 50 and 60 HV isolines spaced *ca.* 2.5–3.0 mm apart. Since 6061 is predominantly a precipitation hardening alloy composition, this result implies that the initial -T6511 temper feedstock is overaged during AFSD deposition. However, the last deposited layer retains *ca.* 30% of the feedstock hardness and the hardness gradient extends over 5 mm, indicating that the thermodynamic state of the deposit continues to change after active deposition is complete.

A second microhardness map was collected overlapping the RS EBSD region of interest (Fig. 3 inset (c)) and is presented in Fig. 5b. The average hardness was 43 ± 2 HV, with values towards the center (42.3 ± 0.9 HV, 11.7–13.0 mm ND) lower than those towards the top and bottom (*e.g.*, 46 ± 2, 11.2–11.5 mm ND). Thus, despite the homogeneous appearance of the hardness map deep in the deposit at the mm-cm length scale, intralayer variations in process history and resulting microstructure result in subtle variation over the 0.1 – 1 mm length scale. We attempted to correlate the spatial variation in hardness to
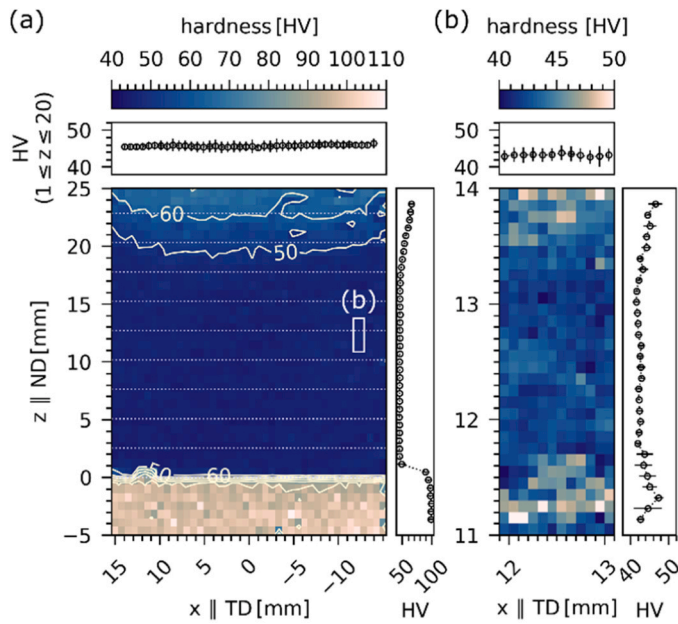
Fig. 5. Vickers hardness map with overlaid iso-hardness contours (-) and notional layer heights (…) relative to the baseplate position (z = 0) measured on a 0.75 mm x 0.75 mm grid (a). The inset region (b) was measured on a 0.1 mm x 0.1 mm grid and positions are given in 100′s of μm.

EBSD-derived quantities including grain size and orientation-averaged Taylor factor, but no compelling correlation was observed (see Supporting Information for further discussion).

3.3. X-ray powder diffraction

A refinement of representative quality is shown in Fig. 6a-b; the complete set of refinements is included in the supplemental information. The refined crystallite size distributions and strain plots are shown in Fig. 6c-d. Key refined parameters are shown in Table 3.

Two characteristics of the material are immediately apparent. First, the observed aluminum possesses a degree of texture, evident in the relative aluminum peak intensities (Fig. 6a) and computed texture index J (Table 3, Appendix 3). Second, the alloy exhibits sharp β-Mg$_2$Si peaks (Fig. 6b) suggesting that the alloy is overaged during deposition. More subtly, size-strain analysis of the observed aluminum diffraction peaks indicates differences in the crystallite size distribution and microstrain present in the three characteristic regions. The lognormal crystallite size distributions ($p(D)$), parameterized by the mean (μ) and standard deviation (σ) of the natural logarithm of the crystallite size distribution (D), refine repeatably to distinctly different distributions (Fig. 6c). The retreating side crystallite size is more sharply distributed over smaller values, while the central region is most shifted towards larger values, yielding mean values $\langle D \rangle$ that differ by a factor of approximately 2.5. The 111 strain plot (*i.e.*, the root mean square variance of the atomic displacement distribution, $\langle \Delta L_{hkl}^2 \rangle^{0.5}$, *vs.* distance L_{hkl}) and model parameters (E_1, E_2, α, β) shows nearly identical curves for the center and retreating side, but markedly lower strain broadening in the advancing side (Fig. 6d).

The differences in apparent crystallite size and microstrain can be understood in relation to the dynamic recovery of the deforming metal. At high temperature the mean subgrain diameter is inversely proportional to the flow stress (σ), which can be expressed as a function of the Zener-Hollomon parameter, sometimes called the temperature-modified strain rate (Appendix 1). [17,60] A smaller crystallite size is obtained either under conditions of larger strain rate or lower temperature (larger Z, σ) during the final increment of strain during AFSD. The differences in
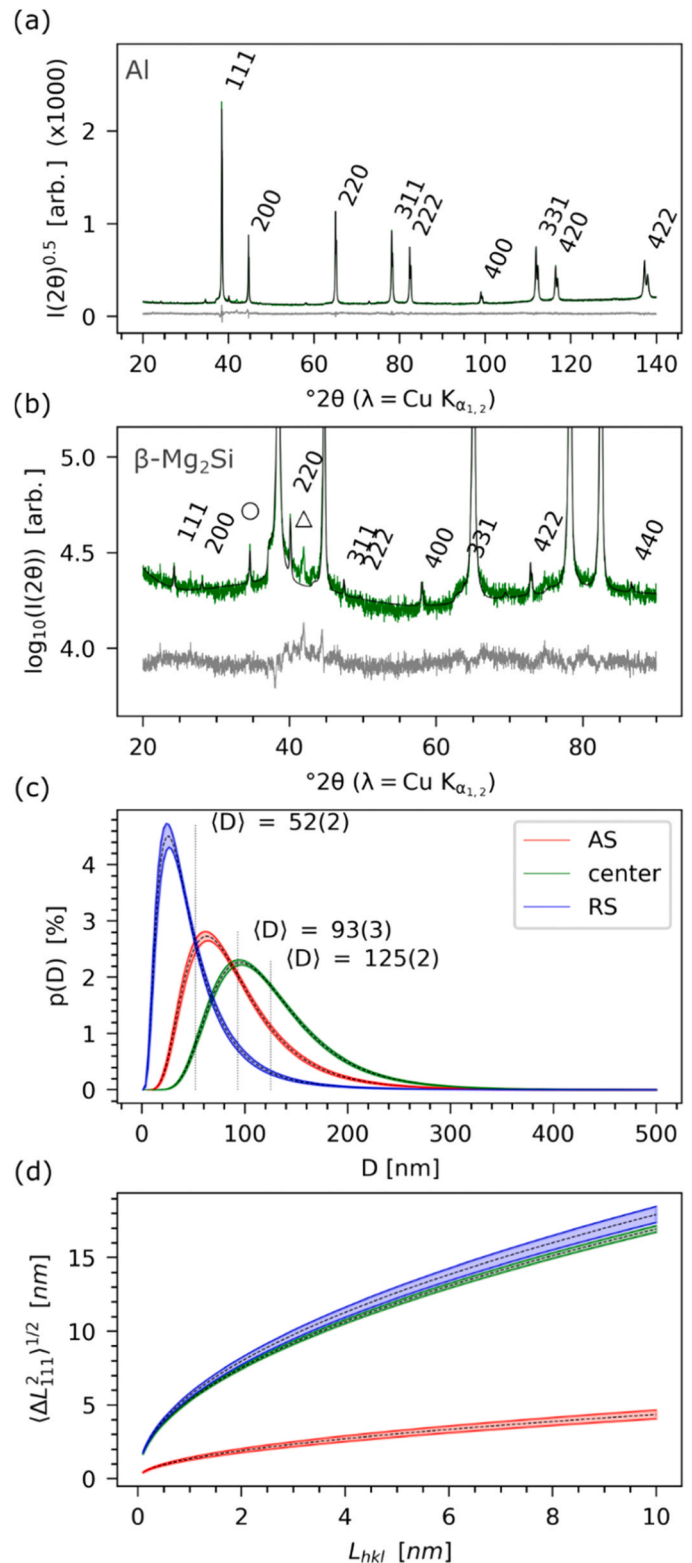

Fig. 6. Rietveld refinement of the center region shows representative fit quality (a), with log-scaled view emphasizing β-Mg$_2$Si phase (○ = K$_\beta$ △ = unknown) (b). The refined log-normal crystallite size distributions for the three characteristic regions (c), and corresponding strain plots for the 111 directions (d) showing estimated values (black lines) and standard error (filled bands). Colors are coded: red (AS), blue (center), green (RS).

Table 3

Rietveld refined parameters and derived quantities. See text and Appendix 3–4 for discussion.

	R_{wp}	a	B_{iso}	μ	σ	E_1	E_2	α	β	† <D>	† J
	[%]	[Å]	[Å²]	[nm]	[nm]	[-]	[-]	[nm]	[-]	[nm]	[-]
AS	7.1	4.05261(1)	0.12(4)	4.40(3)	0.51(1)	1.2(2)	0.7(1)	0.56(8)	0.0034(2)	93(3)	1.182(1)
center	6.2	4.052404(8)	0.71(1)	4.74(2)	0.423(5)	0.069(2)	0.027(2)	13.6(3)	0.028(2)	125(2)	1.191(1)
RS	6.4	4.051923(9)	0.65(3)	3.71(5)	0.69(1)	0.046(3)	0.016(1)	15.5(9)	0.023(1)	52(2)	1.0404(8)

† Derived quantities.

crystallite size distribution therefore implies a transverse gradient in thermomechanical conditions, with larger subgrains and correspondingly smaller values of Z and σ (higher T or lower $\dot{\epsilon}$) present in the deposit center. The differences between strain plots are more difficult to contextualize. The subgrain size is typically understood to vary inversely with dislocation density, where larger dislocation density increases line broadening; consequently, the retreating side should exhibit the largest apparent microstrain broadening and the center should exhibit the least. However, dislocation cores are not the only plausible microstrain mechanism. A more nuanced high-resolution diffraction study employing higher energy (*i.e.*, observing more orders of reflection) would be valuable in investigating this further.

3.4. X-ray pole figure analysis

Pole figure interpretation proceeded first with identification of the SD-SPN local deformation reference frame. By inspection of the ideal shear texture and partial fibers visible in the 111 pole figure and informed by EBSD later performed on subsets of the measurement area, three distinct models were proposed for the three regions of interest. On the retreating side, the closely spaced poles (Fig. 7 g) could be interpreted as either $A/\overline{A}$ or A_1^*/A_2^*. Based in part on the results discussed in the following section, we selected the $A/\overline{A}$ ideal orientations. Thus, our model textures employed $A/\overline{A}$ on the retreating side, $B/\overline{B}$ in the center, and $A/\overline{A}$ and $B/\overline{B}$ on the advancing side, with some partial fiber

apparent in all three regions. The reconstructed 111 pole figures in the sample reference frame, the elucidated local deformation reference frame, and 45° φ₂ ODF sections computed in the local deformation reference frame for the three characteristic regions are presented in Fig. 7. The complete sets of pole figure observations and ODF slices are included in the Supplemental Information.

Material at the deposit center is clearly comparable to the $B/\overline{B}$ ideal shear texture, although interpretation of the direction of material flow is ambiguous because of symmetry and because of the observed sample width. If the elongated poles in Fig. 7d lie along the B fiber, the inferred shear direction is vertical along the sample ND. However, if the elongated pole is a consequence of rigid body rotation over the *ca.* 7 mm TD length observed (see SI for supporting calculation), the sense of deformation is closer to a cylindrical motion coaligned with the tool head. Finally, the texture strength is greatest in the deposit center, and similar but weaker in magnitude on the advancing and retreating sides.

The sense of the transformation between the sample and local deformation reference frame is annotated in Fig. 7. The inferred direction of deformation on the advancing and retreating side is inclined out of the TD-LD plane, consistent with the bowed interface evidenced by metallography in this work (Fig. 3) and reported by others, [8] and by the direction of grain elongation evident in microscopy.

Generally, the texture observed depends both upon the magnitude of shear strain and rigid body rotation, as well as the extent of dynamic recovery and recrystallization. Thus, the local temperature and strain
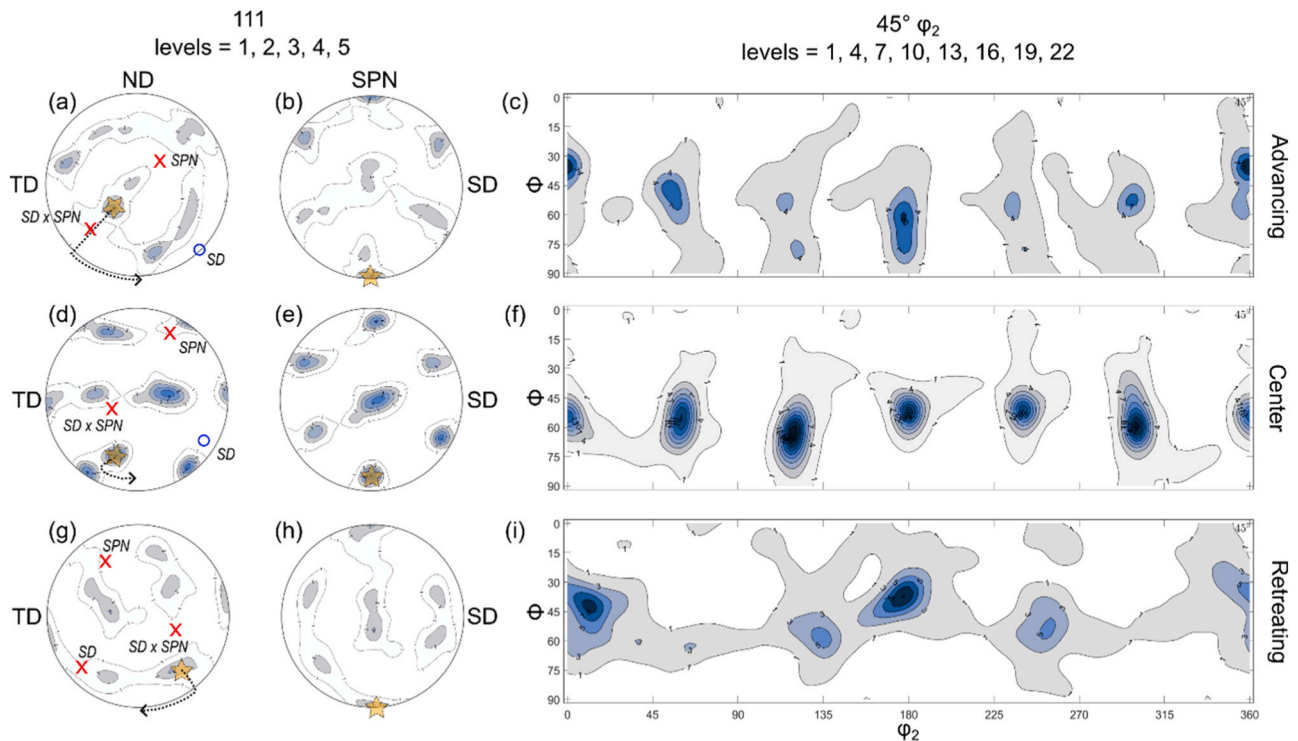
Fig. 7. 111 pole figures in the sample reference frame, transformed into the deformation reference frame, and 45-degree φ₂ sections of the reconstructed ODF transformed to the deformation reference frame: (a-c) advancing side, (d-f) center, (g-i) retreating side. The sense of the transformation is annotated. Note differences in ODF contour level scale on right hand side. The complete ODFs are shown in the SI.

rate play a significant role in determining the final texture. As reported by Montheillet et al. [29,30] for axial torsion at low temperature, the A/$\overline{\text{A}}$ ideal orientations emerge first and the C component becomes stable at large strains. However, at intermediate temperatures and steady-state dynamic recovery the system minimizes the Taylor factor, favoring divergence of grain orientation from the C ideal orientations. At high temperatures (T > 2/3 T_m, where T_m= melting temperature) when continuous dynamic recrystallization dominates, Montheillet et al. report B/$\overline{\text{B}}$ ideal orientations dominate. Following the persistence description of texture formation in polycrystals, [18,30] an untextured polycrystal will upon initial hot torsion accumulate orientations near the A- and B-fibers. Subsequently, divergence in orientation stability results in the accumulation of ideal grain orientations. Similar observations are found in FSW of aluminum. [32] Consequently, we infer the different textures observed across the sample TD are indicative of different thermomechanical process histories, with higher temperatures and strain accumulation in the deposit center, and lower strain accumulation in the extremities for the deposition conditions applied in this study.

Finally, the reconstructed ODF can be used to compute bulk-averaged material properties. For example, given the single crystal elastic stiffness tensor C_{ijmn}, the bulk average is obtained by a simple orientation average [59,77]

$$\langle C_{ijkl} \rangle = \frac{1}{8\pi^2} \int_{SO(3)} a_{im}(g)a_{jn}(g)a_{kp}(g)a_{lq}(g)C_{mnpq}f(g)dg \qquad (1)$$

where $a_{ij}(g)$ are the direction cosines between the crystal axis *i* and sample axis *j*, *g* are orientations in the 3-dimensional rotational orientation space SO(3), and $f(g)$ is the ODF. Projections of the Voigt-averaged Young's modulus for the measured texture components, using reported single crystal elastic tensor values for pure aluminum, [78] are shown in the sample reference frame in Fig. 8 for the three characteristic regions identified in Fig. 3. The texture developed is strongest in the central stir zone; correspondingly, the bulk elastic anisotropy is greatest here as well. The calculated modulus is largest along the weld direction, and smallest at an inclination *ca.* 45° from the WD-TD plane in the BD-WD plane. The texture development is weaker on the advancing and retreating side, where the lowest modulus is computed along the build direction, although perturbed in a fashion commensurate with the direction of plastic flow. The magnitude of the bulk anisotropy is on the order of 1%.

3.5. Electron backscatter diffraction

EBSD was measured near the center of regions analyzed by X-ray pole figure analysis (Fig. 3, inset) to investigate microstructure variations within the thickness of a single layer. The retreating side observation covered an entire repetition of metallographic patterns, while the center and advancing maps collected about half of a layer within a pair of layer boundaries. The EBSD regions on the advancing side and center capture consistent orientation distributions, while the retreating side

differed significantly through the observed layer. These observations are divided by region of interest in the following sections.

3.5.1. Retreating side

The observed EBSD orientation map, grain orientation spread (GOS), and associated texture analysis for the retreating side are presented in Fig. 9. Corresponding optical metallography is also provided. To investigate the apparent changes in microstructure through the layer, the data was sliced into 100 μm segments along ND for grain analysis and 50 μm segments for orientation analysis. Key results are summarized in Fig. 10. Like the X-ray pole figure analysis, ODFs reconstructed from EBSD data display apparent A/$\overline{\text{A}}$ or A_1^*/A_2^* shear texture, with observed partial A- and B-fibers suggesting A/$\overline{\text{A}}$ as the more plausible model. To elucidate the relationship between the sample reference frame and the local deformation reference frame, rotation of the observed ODF was refined against a model comprised of the A- and B-fibers and the two A/$\overline{\text{A}}$ texture components. Starting values for Euler angles were first obtained using the relatively sharp textures near 0–50 μm and 1200–1250 μm ND and the global search algorithm implemented in the MATLAB Global Optimization Toolbox. These values were applied as initial conditions in subsequent least-squares refinement of Euler angles and texture component weights in each segment. Consequently, our results bias the predicted deformation reference frame such that the y-axis contains the unique two-fold axis of the 111 pole figure (Fig. 2). Finally, observation of deformation textures, as opposed to recrystallization textures, indicates extensive dynamic recovery and low driving force for static recrystallization.

Geometrically, treating AFSD as related to hot torsion, we suppose that the direction of macroscopic deformation is tangent to the tool rotation, but is perturbed by the superposition of extrusion and translation upon the system. Material on the front edge of the deposit flows from the advancing to the retreating side, and *vice versa* on the back edge. However, a strain gradient exists beneath the tool, and the deformation recorded in the EBSD image integrates that gradient everywhere underneath the tool. Where material deposited on the front edge is not subsequently deformed beneath the tool, the sense of deformation is AS-to-RS, whereas material deformed by the passing tool may accumulate deformation RS-to-AS beneath the back side of the tool. Projection of the refined $\widehat{SD}$ vector of the local deformation reference frame into the TD-ND plane of the EBSD observation shows such a reversal of likely deformation direction (Fig. 10c) and a corresponding weakening of texture index (Fig. 10d). This analysis oversimplifies the material flow during AFSD, however, and only offers a partial indication of where the tool and prior-layer interfaces might be found.

Additional detail is revealed upon consideration of grain characteristics apparent in the EBSD data. AFSD is a severe plastic deformation process, resulting in spatially heterogeneous temperature, strain, and strain rate distribution. [42] During SPD of aluminum alloys, steady-state grain size resulting from dynamic recrystallization and recovery depends sensitively upon these factors (Appendix 1). Our
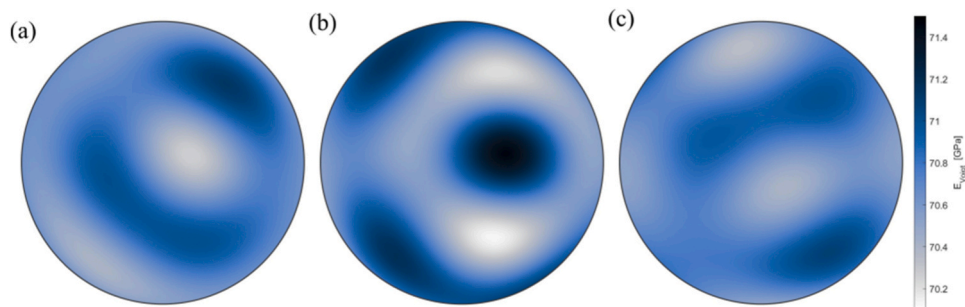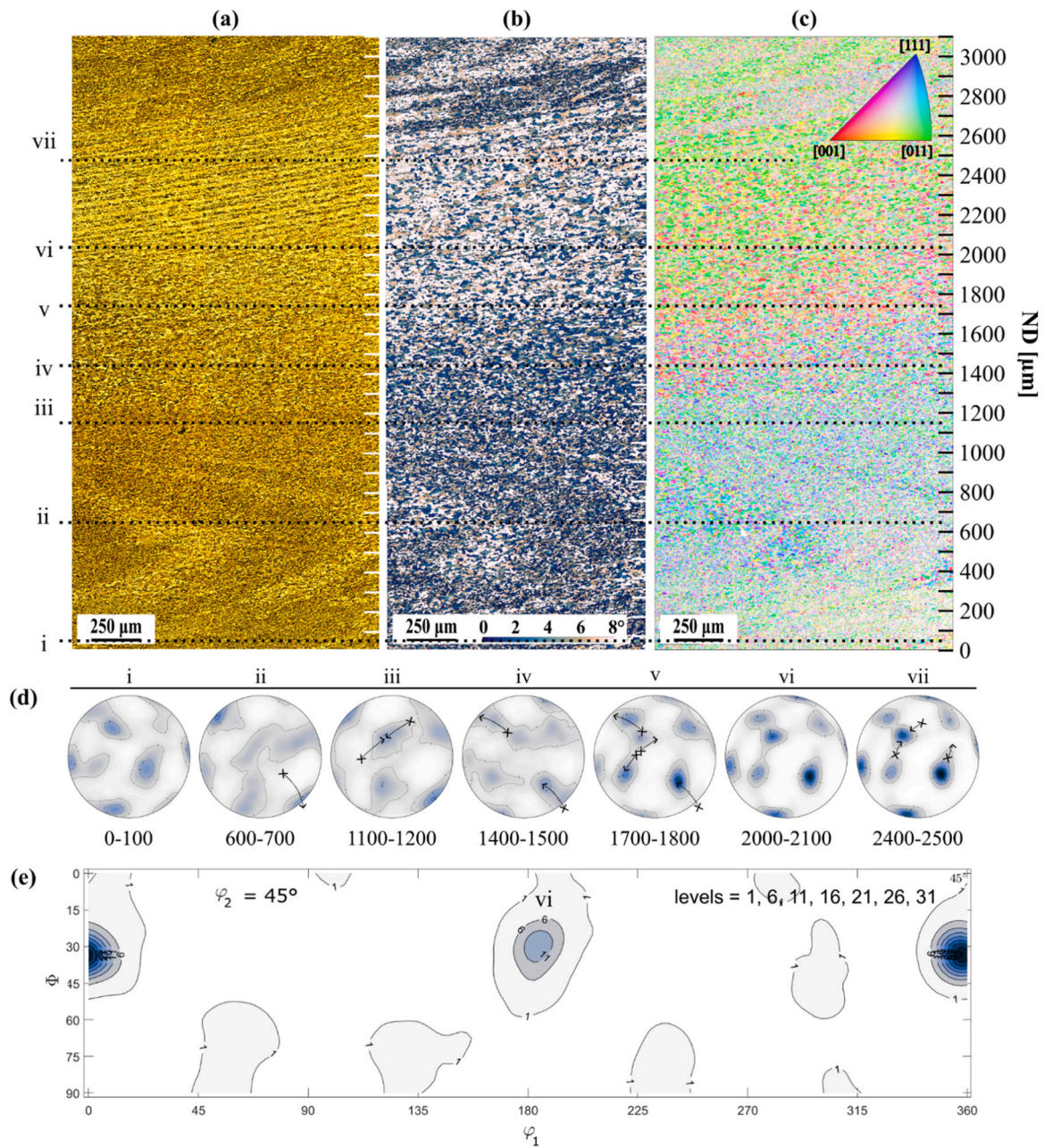

Fig. 8. Voigt-averaged elastic modulus computed using aluminum single crystal elastic tensor components for the (a) advancing side, (b) stir zone, and (c) retreating side.
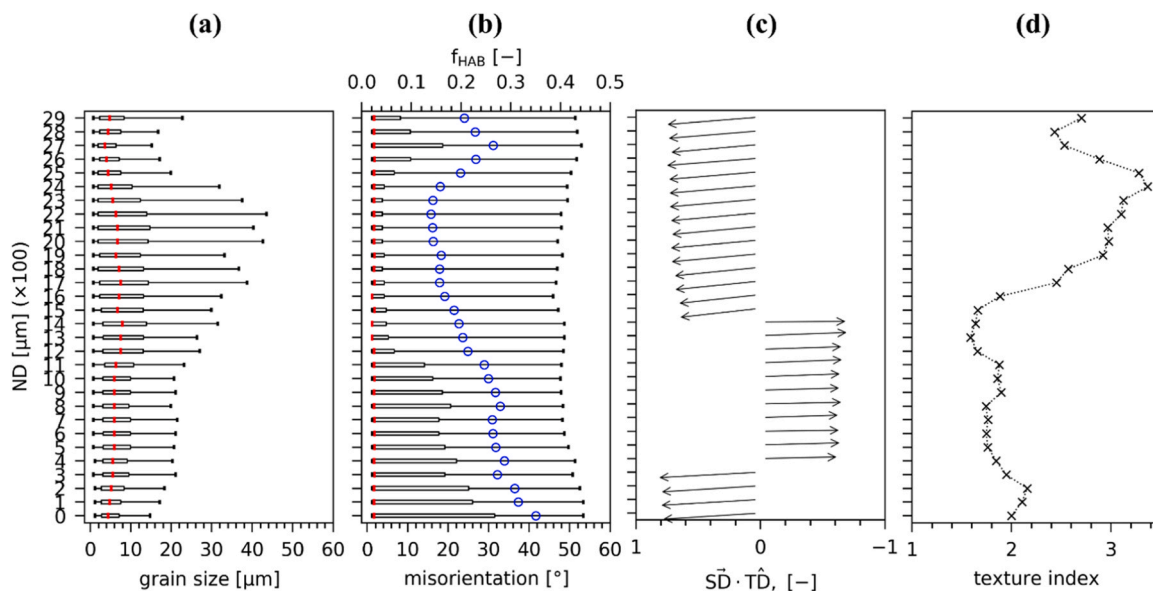
Fig. 9. Retreating side microscopy: optical metallography (a), EBSD grain segmentation and GOS (b), and orientation map with inset IPF key (c). EBSD data were collected with 0.4 μm step size. Select 111 pole figures computed for 50 μm tall slices (d) with the sense of rotation and orientation accumulation annotated (black arrows), and the corresponding reconstructed 45°φ_2 ODF slice at location vi (e). Note that the sample was re-polished between metallography and EBSD observation, so correspondence between (a) and (b-c) is approximate.

inferences from grain characteristics, organized from top to bottom of the RS EBSD region of interest (ROI), are as follows.

Near the top of the ROI (2500–2900 μm) we observe bands of fine grains with low GOS adjacent to coarser grains with high GOS (Fig. 9b). These thin regions of fine grains are less than 100 μm thick and are reminiscent of regions identified by Perry *et al.* in AFSD tracer studies using X-ray computed tomography. [7] Perry *et al.* describe these as microribbons, since they constitute thin bands of fine grains resulting from a combination of elongation and thinning caused by material-protrusion interactions. Tool protrusions are thought to increase the effective strain by compressing material underneath the protrusion and by shearing material along the side of the protrusion. [8] Although the temperature is high, recovery is limited since the protrusions encourage grain refinement within these bands relative to the

surrounding matrix; consequently, the microribbons have a higher number density of high-angle boundaries (HABs), evident in the skew towards HABs evident in our observed misorientation distributions (Fig. 10b). Below this region (1200–2500 μm) the temperature and strain rate remain high, but effective strain is lower without the material-protrusion interaction, so recovery is encouraged which results in larger grains (Fig. 10a) with higher GOS (Fig. 9b). Under mechanisms of cDRX, the misorientation distributions become left-biased by the organization of dislocations into subgrain boundaries (Fig. 10b) and grains are allowed to persist. The texture strength index is greatest near 2400 μm but steadily decreases through this region (Fig. 10d). Continuing to descend (1200–1400 μm), SD appears to rotate around ND, grain size distribution decreases, and misorientation distribution increases (Fig. 10). This appears to be a transition zone, as the adjacent

Fig. 10. Equivalent spherical grain side diameter distribution (a), grain boundary misorientation distribution with fraction HABs (blue circle) (b) estimated deformation direction (c), and texture index (d) for the 30 segmented regions presented in Fig. 7. Note that increased sampling along ND was used in (c) to help reduce distribution of orientations. Box and whiskers indicate the 5th, 25th, 50th, 75th, and 95th percentiles.
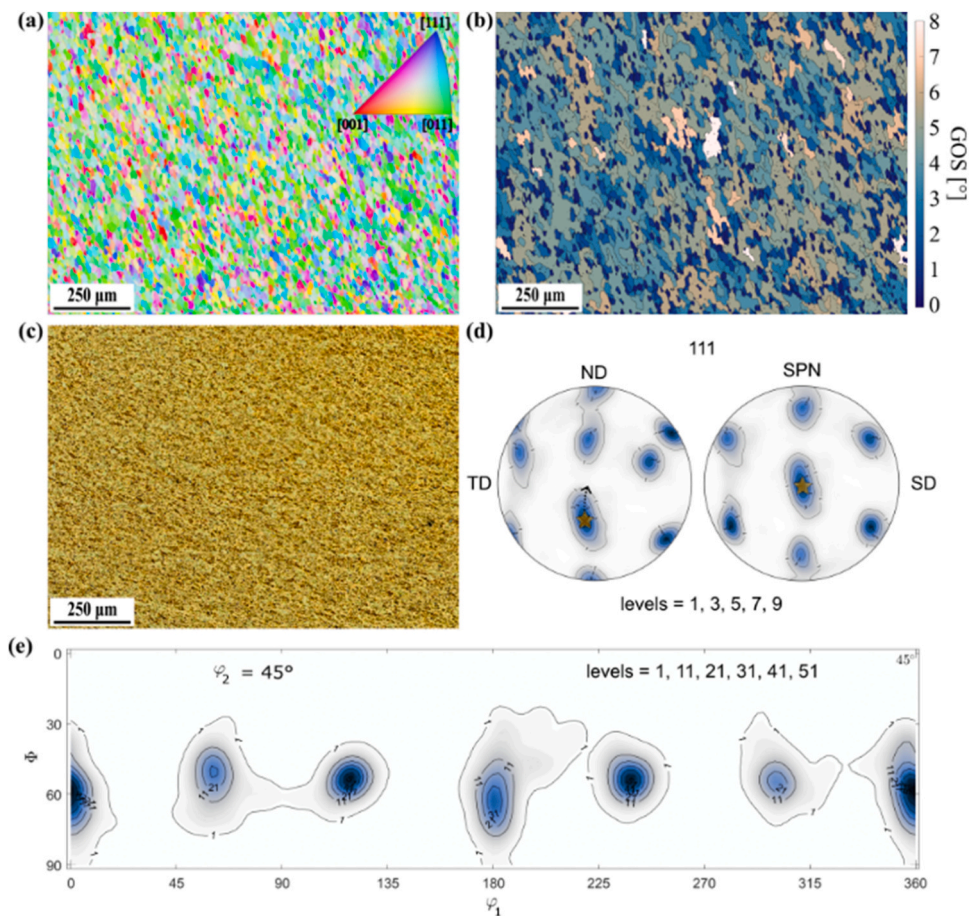
Fig. 11. Center zone microscopy: EBSD orientation map with IPF key (a), grain segmentation and GOS (b), and optical metallography (c). EBSD data were collected with 0.9 μm step size. A representative 111 pole figure reconstructed for a 100 μm tall slice (d) with the sense of rotation annotated (black arrows), and the corresponding reconstructed $45°\varphi_2$ ODF slice (e). Note that the sample was re-polished between metallography and EBSD observation, so correspondence between (a-b) and (c) is approximate.

bands of coarse and fine grains reappear beneath this region. At approximately 500 μm, effective strain is thought to increase by virtue of material-protrusion interactions similarly to the microstructure near the top of the ROI (2500–2900 μm). Similar metallographic, orientation distribution, and grain characteristics reemerge, indicating a full layer was captured. However, the texture index is significantly lower, and the misorientation distributions skew larger, perhaps due to uncontrolled variation in the plasticized volume and peak temperature produced in adjacent layers. [79].

On this evidence, we suggest the likely prior layer interface resides approximately at the 1200 μm mark in Fig. 9c, and that the thermal-mechanical history through the 2.54 mm nominal thickness of the AFSD layer varies substantially depending on the depth relative to the tool interface.

3.5.2. Central region

A comparison of optical metallography with the observed EBSD orientation map, grain segmentation and GOS map, and associated texture analysis for the specimen center is presented in Fig. 11. The computed 111 pole figure (Fig. 11d) and 45° φ_2 ODF (Fig. 11e) are presented as well. In this field of view the texture is similar throughout the ND, exhibiting predominantly B/$\overline{\text{B}}$ ideal shear texture components and weak B-fiber.

Accumulation of orientations from the B-fiber into an ideal shear texture indicates a large magnitude of accumulated strain. By inspection of the 111 pole figure in both the specimen and local deformation reference frames (Fig. 11d), it is apparent that the shear direction is nearly coaligned with the transverse direction in this particular field of view. In contrast with the AS and RS, the deposit center distributes orientations over the B-fiber with ⟨110⟩ oriented close to the transverse direction. In the analysis of Toth, [18] the B-fiber results in double slip along the primary FCC slip system, with balanced double slip for the C ideal orientation and unbalanced double slip at the B ideal orientation and elsewhere along the fiber. Once obtained, the B ideal orientation is highly stable; correspondingly, the largest overall texture index is observed in this region (*ca.* 3.4). Again, observation of a sharp deformation texture suggests the majority of microstructure development occurs dynamically during hot deformation and not statically thereafter.

Unlike the retreating side observation, the IPF map (Fig. 11a) shows an absence of strong texture gradients and the GOS map (Fig. 11b) show a relatively uniform distribution of incompletely recovered grains. This implies more uniform plasticization and an absence of the flow localization apparent on the retreating side EBSD observation (Fig. 9c) and in optical metallography (Fig. 3-Fig. 4). The grain size distribution and grain misorientation distribution for the center region are presented in Fig. 12. The grain size distribution is significantly larger and more uniform along ND than those observed in the retreating region. Typical median and interquartile ranges for the center region are 16^{+11}_{-9} μm, compared with 6^{+5}_{-3} μm on the retreating side. The misorientation distributions are similarly uniform and strongly left-biased with > 60% low-angle grain boundaries (LABs), but with significant skew towards HABs. Assuming the observed grain development is due to continuous dynamic recrystallization, the larger relative grain size suggests deformation occurs at a lower value of Z (*i.e.*, lower strain rate and/or higher temperature) than the neighboring retreating zone (Appendix 1).

3.5.3. Advancing side

The observed EBSD orientation map and reconstructed grain map and grain orientation spread (GOS) is compared with optical metallography of the same region in Fig. 13. The orientation distribution for 100 μm tall slices along the normal direction shows essentially no difference in this field of view; a representative 111 pole figure and 45° φ_2 ODF slice is shown in Fig. 13(d) and (e) respectively. These exhibit a distribution of orientations along the A-fiber. After initial deformation by hot torsion from an unoriented grain assembly, orientations first
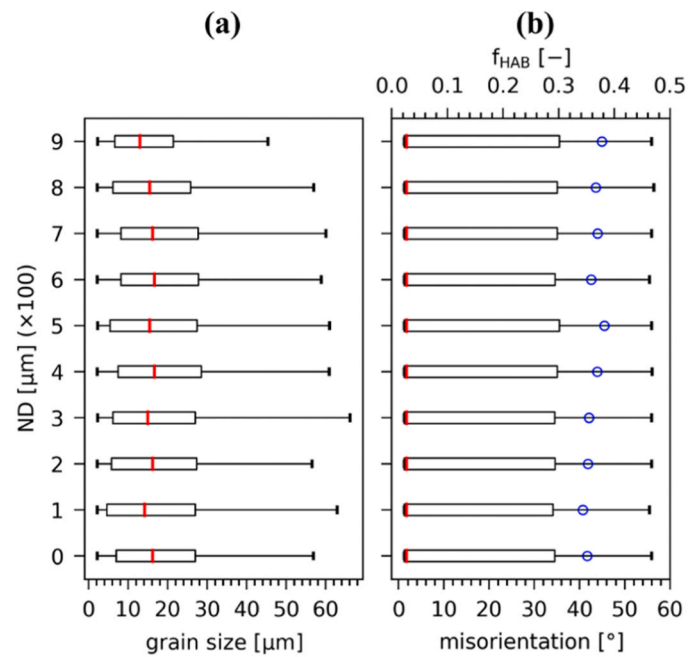

Fig. 12. Central zone grain equivalent spherical diameter (a), and grain boundary misorientation angle with fraction HABs (blue circle) (b). Box and whiskers indicate the 5th, 25th, 50th, 75th, and 95th percentiles.

move in Euler space towards the A- and B-fibers along the direction of rotation and then begin to accumulate into the relatively stable ideal orientations for slip on the FCC {111}⟨110⟩ system. [18] The relative distribution of orientations along the A-fiber observed here suggests a relatively low strain accumulation, although a quantitative assessment is not feasible from this analysis. Moreover, in the persistence model of shear texture development during plastic deformation, [18] the A_2^* orientation is expected to accumulate a larger grain population than the A_1^* orientation following initial deformation due to differing divergence in the plastic grain rotation rate; the integrated orientation space near A_2^* and A_1^* in Fig. 13(e) does appear to exhibit this inequality.

Like the center observation, the IPF map (Fig. 13a) shows an absence of strong texture gradients and the GOS map (Fig. 13b) show a relatively uniform distribution of incompletely recovered grains. The segmented GOS map appears in Fig. 13, and the grain size distribution and grain misorientation distribution for the advancing side are presented in Fig. 14. Like in the center, the grain size distribution is significantly larger and more uniform along ND than is observed in the retreating region. Typical median and interquartile ranges for the advancing region are 15^{+13}_{-10} μm, compared with 6^{+5}_{-3} μm on the retreating side. The misorientation distributions are again uniform along the normal direction, strongly left-biased with > 60% LABs, but with significant skew towards HABs. Again, this implies microstructure development in this region of the advancing side occurs at lower values of Z than the region of the retreating side studied in this work.

3.6. Combined interpretation

Comparison of microstructure observations spanning multiple length scales demonstrates the importance of adopting a comprehensive approach to materials characterization of AFSD articles. Because X-ray pole figure analysis averages over multiple layers and the plastic deformation throughout the illuminated volume is not homogeneous, the resulting texture analysis is somewhat more difficult to interpret. However, EBSD analysis over *ca.* 1 mm² in the advancing side and center did not span the entire layer height and does not capture the full range of microstructures developed in those regions, leading to subtly different
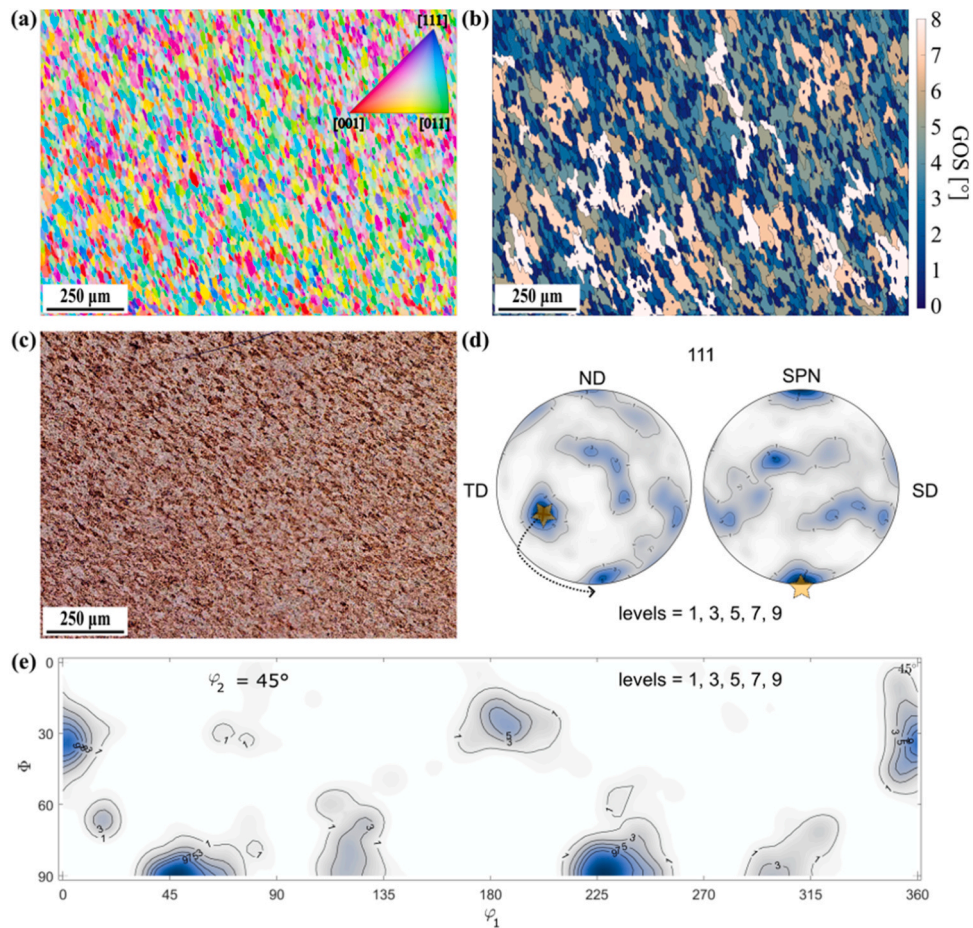
Fig. 13. Advancing side microscopy: EBSD orientation map with IPF key (a), grain segmentation and GOS (b), and optical metallography (c). EBSD data were collected with 0.4 μm step size. A representative 111 pole figure reconstructed for a 100 μm tall slice (d) with the sense of rotation annotated (black arrows), and the corresponding reconstructed 45°φ₂ ODF slice (e). Note that the sample was re-polished between metallography and EBSD observation, so correspondence between (a-b) and (c) is approximate.

texture interpretation between the pole figure and EBSD analyses. Pole figure and EBSD analysis both suggest bulk anisotropy in the AFSD deposit at cm- and sub-mm length scales, respectively. Finally, panoramic metallography offers a view of where and how microstructure features generated during AFSD vary and repeat across the full TD-ND cross section, and hardness mapping offers a proxy for the spatial variation of the thermodynamic state of the precipitation hardening alloy. Taken together, these observations demonstrate there is subtle heterogeneity across mm-cm length scales, including intralayer microstructure variability, transverse process asymmetry, and continued microstructure development of the ultimate layers after active deposition.

There are at least two detailed reports of computational modeling of AFSD aluminum 6061 with important implications for this work. The smoothed particle hydrodynamics (SPH) methods of Stubblefield *et al.* predict transverse asymmetry in the thermomechanical conditions generated during deposition, a larger strain accumulation in the deposit centerline, and predict a w-shaped temperature profile beneath the tool in the TD-ND plane. [39,40] Gotawala & Yu produce computational fluid dynamics (CFD) results that predict spatially heterogeneous strain rate ($\dot{\varepsilon}$) and temperature (T) distributions in the TD-ND plane. [42] Calculation of the dependent Zener-Hollomon parameter and flow stress (σ) result in a nearly uniform value in the TD-ND plane beneath the tool to a depth of 3 mm, and consequently a dynamic viscosity ($\mu = \sigma/3\dot{\varepsilon}$) that varies proportionally with the strain rate. Since grain size during dynamic recrystallization is found to vary inversely with the flow stress (Appendix 1) Gotawala & Yu assert that their finding validates prediction of homogeneous microstructure development during AFSD.

Importantly, these two modeling studies and this report study different material deposition rates. All three report results for 300 rpm tool speed, however Gotawala & Yu simulate 1 mm thick layers, [42] Stubblefield *et al.* study 1.5 mm thick layers, [39] and we produce 2.54 mm thick layers. In each case the travel rate (V) was near 2 mm·s⁻¹, but the feed rate (F) varied considerably (0.67, 2.11, and 2.54 mm·s⁻¹, respectively). According to the analysis of Stubblefield *et al.* where F = 2.11 mm·s⁻¹ is identified as the optimal feed rate, and scaling by relative layer height, both Gotawala & Yu and this report assess material produced in the starved condition, which Stubblefield *et al.* predict will result in a more heterogeneous microstructure. [39] Thus, the results of this study would seem to contradict Gotawala & Yu, but support the inference of heterogeneity and transverse asymmetry reported by Stubblefield *et al.* This meta-analysis remains somewhat ambiguous of course, given that the machine inputs were not controlled for between studies and that correlation between layer height, feed rate, and the resulting thermal-mechanical state likely exists.

The resulting microstructural heterogeneity may influence anisotropy in bulk strength as well as localized yielding behavior. In our earlier case study of AFSD Ti-64 subscale tensile coupons, localized plastic deformation was found to correlate with the AFSD generated microstructure and texture. [80] Others have noted failure at buried interfaces affecting through-thickness strength, [43] and that mechanical properties depend upon process variability during deposition of complex shapes. [11] Another study exploring neutron imaging of AFSD 6061 reported varying ultimate tensile strength and reduced strain at failure (ε_f) of normal-direction tensile coupons extracted beneath the
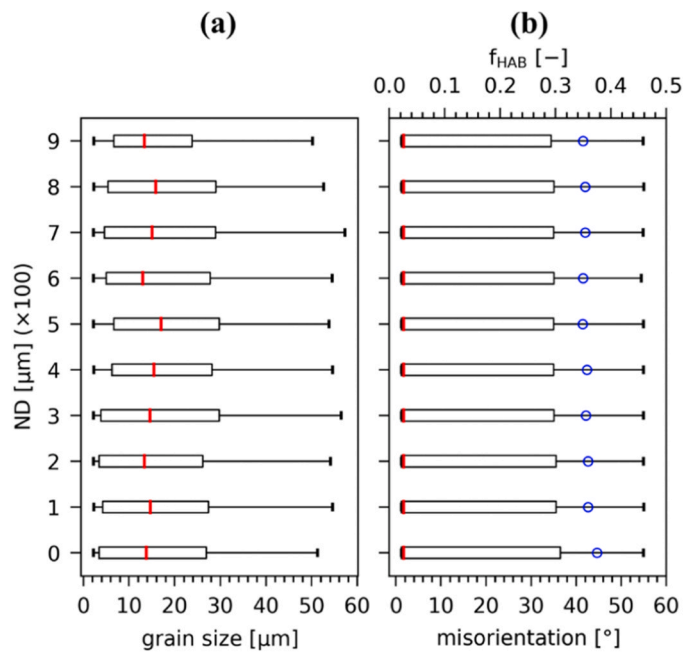
Fig. 14. Advancing side grain equivalent spherical diameter (a), and grain boundary misorientation angle with fraction HABs (blue circle) (b). Box and whiskers indicate the 5th, 25th, 50th, 75th, and 95th percentiles.

tool protrusion (*ca.* 90% ε_f), and in the flash region (*ca.* 50% ε_f) compared with the deposit center line. [81] The extent to which heterogeneity can be accommodated in different engineering applications should be considered in assessing whether AFSD parts are suitable replacements for their conventionally formed counterparts.

Finally, the as-deposited microstructure plays a significant role in subsequent development during heat treatment, as is typically applied to aluminum 6061 to reach target mechanical properties. In friction stir welding of aluminum alloys, for example, it has been noted that over-aging in the weld zone combined with fine grain size distribution leads to unstable grain boundaries without coherent dispersoids to pin grain boundary motion, resulting in extreme abnormal grain growth during heat treatment. [82] The ability of AFSD to produce grain refinement is undoubtedly useful, but the resultant microstructure must be considered holistically in context of the target product to produce optimal parts. This may sharply limit the process window of legacy alloys designed for traditional forming methods in ways that are not obvious.

4. Conclusions

This work demonstrates that additive friction-stir deposition of aluminum alloy 6061 may result in spatial heterogeneity across multiple length scales. The key findings may be summarized:

- Metallography of the TD-ND plane exhibits transverse asymmetry evident in strain-rate and temperature-sensitive flow localization and grain characteristics.
- Hardness mapping at 0.750 mm spatial resolution indicates the thermodynamic state of the hardening precipitates continues to develop after active deposition, and at 0.100 mm spatial resolution reveals intralayer variation in the retreating side of the deposit.

- Line profile analysis of powder X-ray diffraction data shows different coherent domain size distributions, with mean values: center 125(2) nm, advancing 93(3) nm, and retreating zone 52(2) nm (mean and standard error). This trend matches EBSD grain statistics: center $16^{+11}_{-9}\mu$m, advancing $15^{+13}_{-10}\mu$m, and retreating 6^{+5}_{-3} µm (median $\pm$ interquartile).
- X-ray pole figure and EBSD analyses demonstrate distinct texture development in the center (sharp $B/\overline{B}$) advancing ($A/\overline{A}$, A-fiber), and retreating ($A/\overline{A}$, various fiber) zones.
- Strong texture in the deposit center predicts percent-level bulk anisotropy in Young's modulus.
- EBSD texture analysis on the retreating side indicates intralayer variation in the direction and magnitude of accumulated shear strain.
- EBSD grain analysis on the retreating side reveals intralayer variation in grain size and grain misorientation that, together with hardness mapping, suggests non-uniform thermal-mechanical history through the deposited layer thickness.

The ability to repeatably control microstructure development underpins control of engineering properties in structural alloys. Controlling or mitigating the process heterogeneity that appears characteristic of additive friction stir deposition would seem a necessary step to broaden deployment in real-world applications and may define limitations for this deposition technique.

Declaration of Competing Interest

The authors declare that they have no known competing financial interests or personal relationships that could have appeared to influence the work reported in this paper.

Data availability

Data will be made available on request.

Appendix 1. Zener-Hollomon parameter

The balance of a metal's level of deformation, dynamic recovery, and dynamic recrystallization during hot deformation is related to the Zener-

Holloman parameter. The Zener-Holloman parameter (Z) is a constitutive relationship between strain-rate ($\dot{\varepsilon}$) and temperature (T) for the purposes of understanding a metal's flow-stress response to a specific thermomechanical regime. Its form is given as [60]

$$Z = \dot{\varepsilon}\exp\frac{Q}{RT}. \tag{A1.1}$$

Since the equation has rate dependance, Q is an activation energy for deformation, and for 6061, it is calculated from empirical studies as 196 [kJ/mol]. [83] Recrystallization mechanisms are responsible for lowering the flow stress of a metal under continued deformation, and at certain temperatures and strain rates, the method of recrystallization changes depending on the stacking-fault energy of the metal as well. [17] The relationship between Zener-Holloman parameter and the flow stress (σ) is given as [17,60]

$$Z = c_1\sinh(\sigma c_2)^n, \tag{A1.2}$$

where c_1, c_2, and n are material constants. At low stress, this relationship can be reduced to [17]

$$Z = c_3\sigma^m, \tag{A1.3}$$

where c_3 and m are material constants. Higher values of Z are thus associated with higher flow stress, which correlates to a higher dislocation density, and increasing the driving force for nucleation of new grains.

Finally, at large strains under severe hot plastic deformation it is found that subgrain size (D) approaches a steady state. [17] In aluminum this has been empirically found to vary inversely with the logarithm of Z [17]

$$D = K_1 - K_2\ln(Z) = K_1 - K_2\ln(\dot{\varepsilon}) - K_2\frac{Q}{RT}, \tag{A1.4}$$

where K_1 and K_2 are empirical constants. Process maps for Eqs. A1.1 and A1.4 are included in the supplemental information. This is related to the Derby relationship. [84]

$$\frac{\sigma}{\mu}\left(\frac{D}{b}\right)^{\frac{2}{3}} = K, \tag{A1.5}$$

in which the grain size during dynamic recrystallization is inversely proportional to the flow stress (σ) through the shear modulus (μ), Burgers vector (b) and a material constant K (approximately 10 for FCC metals).

Appendix 2. Texture rotation

As noted above, the first step in texture analysis of materials for which the deformation is undefined with reference to the machine reference frame is determining the orientation of the local deformation reference frame. This work explored the built-in algorithm `centerSpecimen' provided with MTEX, as well as a model-based strategy for identifying the local deformation reference frame. The symmetry-based `centerSpecimen' algorithm attempts to identify two orthogonal vectors containing two mirror planes of orthorhombic symmetry in the ODF and subsequently computes the rotation aligning these two vectors with the x- and y- Cartesian axes. In the model-based approach, we defined likely model ODFs containing the A- and B-fibers and possible ideal deformation textures (Table 2.) and refined the rotation bringing the observed ODF into coincidence with the model. The symmetry-based approach proved problematic because the textures present are not necessarily self-symmetric, and the implementation proved insensitive to weak features like fiber location.

The solution space of the refined rotation is degenerate due to symmetry of the crystalline phase, *i.e.* here FCC with Fm$\overline{3}$m space group. Particularly, the $A/\overline{A}$ and A_1^*/A_2^* ideal orientations are related by a 30° rotation on the A fiber and so are only differentiated by the location of the B fiber or other ideal textures. Our naïve assumption is that the two key fiber axes (*i.e.,* SPN $\|$ {111} and SD $\|$ {110}) are closely related to the rotational axis and tangent direction of the machine tool. This assumption was used to bias the refinement.

Finally, rigid body rotation over the viewed area can introduce additional orientation distribution in the observed data. This effect is pronounced in the X-ray pole figure observations, but minimal in the EBSD observations (see SI for supporting calculations).

Appendix 3. Texture index

Both the X-ray diffraction analysis and texture analysis presented in this paper refer to a quantity called the texture index. The texture index (J) is a quantitative measure of the severity of the texture, which can be computed from the orientation distribution function f(g) [59]

$$J = \oint_{SO(3)} [f(g)]^2 dg, \tag{A3.1}$$

or, when using a symmetrized spherical harmonic expansion of f(g),

$$J = \sum_{l,u,v}\frac{1}{2l+1}|C_l^{uv}|^2. \tag{A3.1}$$

J takes a value of 1 when the orientation distribution is random and diverges to infinity for the case of an ideal single crystal.

Appendix 4. Diffraction line broadening

The whole powder pattern modeling (WPPM) approach to line broadening analysis in powder diffraction is based upon the Fourier convolution theorem, [85] whereby the observed diffracted intensity distribution ($I_{hkl}(S)$, $S = s - s_0$, s = 2 sin(θ) / λ) is expressed as the convolution of the instrument resolution function ($T^{IP}(L)$) and terms representing crystallographic imperfections including finite size ($A^S(L)$) and atomic displacement ($A^D(L)$)

$$I_{hkl}(S) \propto \int T^{IP}(L) A^S(L) A^D(L) \dots \exp(2\pi i L S) \; dL, \tag{A4.1}$$

where L is the Fourier length in direct space and S is correspondingly a length in reciprocal space.

For size broadening, this work assumes a lognormal spherical crystallite size distribution. This is, of course, an oversimplification of the real subgrain structure present in the specimen. The size (D) distribution ($p(D)$) is parameterized by the lognormal mean (μ) and standard deviation (σ)

$$p(D) = \frac{1}{D\sigma\sqrt{2\pi}} \exp\left[-\frac{1}{2} \frac{(\ln D - \mu)^2}{\sigma^2} \right]. \tag{A4.2}$$

Averaging over the Fourier transform of the intensity scattered by a spherical crystal, weighted by $p(D)$, yields an analytic expression for $A^S(L)$ [85]

$$A^S(L) = \sum_{n=0}^{3} H_n \frac{M_{3-n}}{2M_3} \; erfc\left[\frac{\ln(KL) - \mu - (3-n)\sigma^2}{\sigma\sqrt{2}} \right] L^n, \tag{A4.3}$$

where H_n and K are constants depending upon crystallite shape and M_i are the ith moments of $p(D)$.

Line broadening from lattice distortions, often referred to as microstrain broadening, may arise from any microscopic mechanism resulting in an atomic displacement field over a coherently scattering domain. The case for planar defects in metals, including faulting and dislocations, has been well developed; however, in the microstructure resulting from severe plastic deformation, one might anticipate many types of crystal imperfection contribute to the total observed microstrain broadening. The Popa-Adler-Houska (PAH) [86–88] model of microstrain broadening discards physical models of lattice strain in favor of empirical parameterization [55,56]

$$\langle \Delta L_{hkl}^2 \rangle_{PAH} = \Gamma_{hkl}\left(\alpha L + \beta L^2 \right), \tag{A4.4}$$

where for cubic crystals, [86]

$$\Gamma_{hkl} = A + B \frac{\left(h^2 k^2 + k^2 l^2 + l^2 h^2 \right)}{\left(h^4 + k^4 + l^4 \right)}. \tag{A4.5}$$

In this formulation, the length (L) dependence of the strain field (ΔL_{hkl}) is determined by the coefficients α and β, and the elastic anisotropy is determined by the quantity Γ_{hkl} and its coefficients A and B. In the notation of Popa, [86] $A = E_1$ and $B = 2E_2$, where the values of E_i are related to the crystal elastic tensor. The corresponding strain broadening term $A^D(L)$ is [55,56,88]

$$A_{hkl}^D(L) = \exp\left[-2\pi^2 s^2 \langle \Delta L_{hkl}^2 \rangle \right]. \tag{A4.6}$$

These models have been implemented in the Rietveld software package TOPAS [52,55] and are distributed with the software as of version 7. Additional references on the topic of microstructural line broadening in powder X-ray diffraction are available, for example, in [89–91] and references therein.

References

[1] R.S. Mishra, R.S. Haridas, P. Agrawal, Friction stir-based additive manufacturing, Sci. Technol. Weld. Join. 27 (2022) 141–165, https://doi.org/10.1080/13621718.2022.2027663.

[2] H.Z. Yu, M.E. Jones, G.W. Brady, R.J. Griffiths, D. Garcia, H.A. Rauch, C.D. Cox, N. Hardwick, Non-beam-based metal additive manufacturing enabled by additive friction stir deposition, Scr. Mater. 153 (2018) 122–130, https://doi.org/10.1016/j.scriptamat.2018.03.025.

[3] N. Tuncer, A. Bose, Solid-state metal additive manufacturing: a review, Jom 72 (2020) 3090–3111, https://doi.org/10.1007/s11837-020-04260-y.

[4] R. Motallebi, Z. Savaedi, H. Mirzadeh, Additive manufacturing – a review of hot deformation behavior and constitutive modeling of flow stress, Curr. Opin. Solid State Mater. Sci. 26 (2022) 100992, https://doi.org/10.1016/j.cossms.2022.100992.

[5] H.Z. Yu, R.S. Mishra, Additive friction stir deposition: a deformation processing route to metal additive manufacturing, Mater. Res. Lett. 9 (2021) 71–83, https://doi.org/10.1080/21663831.2020.1847211.

[6] H.Z. Yu, Additive Friction Stir Deposition, Elsevier,, 2022, https://doi.org/10.1016/C2020-0-01505-7.

[7] M.E.J. Perry, H.A. Rauch, R.J. Griffiths, D. Garcia, J.M. Sietins, Y. Zhu, Y. Zhu, H. Z. Yu, Tracing plastic deformation path and concurrent grain refinement during additive friction stir deposition, Materialia 18 (2021) 101159, https://doi.org/10.1016/j.mtla.2021.101159.

[8] M.E.J. Perry, R.J. Griffiths, D. Garcia, J.M. Sietins, Y. Zhu, H.Z. Yu, Morphological and microstructural investigation of the non-planar interface formed in solid-state metal additive manufacturing by additive friction stir deposition, Addit. Manuf. 35 (2020) 101293, https://doi.org/10.1016/j.addma.2020.101293.

[9] D.Z. Avery, B.J. Phillips, C.J.T. Mason, M. Palermo, M.B. Williams, C. Cleek, O. L. Rodriguez, P.G. Allison, J.B. Jordon, Influence of grain refinement and microstructure on fatigue behavior for solid-state additively manufactured Al-Zn-Mg-Cu alloy, Metall. Mater. Trans. A Phys. Metall. Mater. Sci. 51 (2020) 2778–2795, https://doi.org/10.1007/s11661-020-05746-9.

[10] B.A. Rutherford, D.Z. Avery, B.J. Phillips, H.M. Rao, K.J. Doherty, P.G. Allison, L. N. Brewer, J.Brian Jordon, Effect of thermomechanical processing on fatigue behavior in solid-state additive manufacturing of Al-Mg-Si alloy, Metals 10 (2020) 1–17, https://doi.org/10.3390/met10070947.

[11] C.J.T. Mason, R.I. Rodriguez, D.Z. Avery, B.J. Phillips, B.P. Bernarding, M. B. Williams, S.D. Cobbs, J.B. Jordon, P.G. Allison, Process-structure-property relations for as-deposited solid-state additively manufactured high-strength aluminum alloy, Addit. Manuf. 40 (2021) 101879, https://doi.org/10.1016/j.addma.2021.101879.

[12] B.J. Phillips, C.Jacob Williamson, R.P. Kinser, J.Brian Jordon, K.J. Doherty, P. G. Allison, Microstructural and mechanical characterization of additive friction stir-deposition of aluminum alloy 5083 effect of lubrication on material anisotropy, Materials 14 (2021) 6732, https://doi.org/10.3390/ma14216732.

[13] K. Anderson-Wedge, D.Z. Avery, S.R. Daniewicz, J.W. Sowards, P.G. Allison, J. B. Jordon, R.L. Amaro, Characterization of the fatigue behavior of additive friction stir-deposition AA2219, Int. J. Fatigue 142 (2021) 105951, https://doi.org/10.1016/j.ijfatigue.2020.105951.

[14] Y. Li, B. Yang, M. Zhang, H. Wang, W. Gong, R. Lai, Y. Li, J. Teng, The corrosion behavior and mechanical properties of 5083 Al-Mg alloy manufactured by additive friction stir deposition, Corros. Sci. 213 (2023) 110972, https://doi.org/10.1016/j.corsci.2023.110972.

[15] H.J. McQueen, S. Spigarelli, M.E. Kassner, E. Evangelista, Hot Deformation and Processing of Aluminum Alloys, CRC Press,, 2016, https://doi.org/10.1201/b11227.

[16] T.D. State, Recovery, recrystallization, and grain-growth structures, ASM Handb. (2005) 552–562, https://doi.org/10.31399/asm.hb.v14a.a0004019.

[17] A. Rollett, G.S. Rohrer, J. Humphreys. Recrystallization and Related Annealing Phenomena, third ed., Elsevier,, 2017 https://doi.org/10.1016/j.matchar.2020.110382.

[18] L.S. Tóth, K.W. Neale, J.J. Jonas, Stress response and persistence characteristics of the ideal orientations of shear textures, Acta Met. 37 (1989) 2197–2210, https://doi.org/10.1016/0001-6160(89)90145-4.

[19] I.J. Beyerlein, L.S. Tóth, Texture evolution in equal-channel angular extrusion, Prog. Mater. Sci. 54 (2009) 427–510, https://doi.org/10.1016/j.pmatsci.2009.01.001.

[20] L.S. Tóth, Texture evolution in severe plastic deformation by equal channel angular extrusion, Adv. Eng. Mater. 5 (2003) 308–316, https://doi.org/10.1002/adem.200310084.

[21] R. Arruffat-Massion, S. Suwas, L.S. Tóth, W. Skrotzki, J.-J. Fundenberger, A. Eberhardt, Experiments and modelling of ECAE textures of f.c.c. polycrystals, Mater. Sci. Forum 495–497 (2005) 839–844, https://doi.org/10.4028/www.scientific.net/msf.495-497.839.

[22] S. Li, I.J. Beyerlein, M.A.M. Bourke, Texture formation during equal channel angular extrusion of fcc and bcc materials: comparison with simple shear, Mater. Sci. Eng. A 394 (2005) 66–77, https://doi.org/10.1016/j.msea.2004.11.032.

[23] I.J. Beyerlein, C.N. Tomé, Analytical modeling of material flow in equal channel angular extrusion (ECAE), Mater. Sci. Eng. A 380 (2004) 171–190, https://doi.org/10.1016/j.msea.2004.03.063.

[24] I.J. Beyerlein, S. Li, C.T. Necker, D.J. Alexander, C.N. Tomé, Non-uniform microstructure and texture evolution during equal channel angular extrusion, Philos. Mag. 85 (2005) 1359–1394, https://doi.org/10.1080/09500830500040940.

[25] S. Li, I.J. Beyerlein, D.J. Alexander, S.C. Vogel, Texture evolution during multi-pass equal channel angular extrusion of copper: Neutron diffraction characterization and polycrystal modeling, Acta Mater. 53 (2005) 2111–2125, https://doi.org/10.1016/j.actamat.2005.01.023.

[26] S. Li, I.J. Beyerlein, D.J. Alexander, S.C. Vogel, Texture evolution during equal channel angular extrusion: effect of initial texture from experiment and simulation, Scr. Mater. 52 (2005) 1099–1104, https://doi.org/10.1016/j.scriptamat.2005.02.008.

[27] S. Suwas, R. Arruffat Massion, L.S. Tóth, J.J. Fundenberger, B. Beausir, Evolution of texture during equal channel angular extrusion of commercially pure aluminium: experiments and simulations, Mater. Sci. Eng. A 520 (2009) 134–146, https://doi.org/10.1016/j.msea.2009.05.028.

[28] G.R. Canova, U.F. Kocks, J.J. Jonas, Theory of torsion texture development, Acta Met. 32 (1984) 211–226, https://doi.org/10.1016/0001-6160(84)90050-6.

[29] F. Montheillet, M. Cohen, J.J. Jonas, Axial stresses and texture development during the torsion testing of Al, Cu and α-Fe, Acta Met. 32 (1984) 2077–2089, https://doi.org/10.1016/0001-6160(84)90187-1.

[30] F. Montheillet, P. Gilormini, J.J. Jonas, Relation between axial stresses and texture development during torsion testing: a simplified theory, Acta Met. 33 (1985) 705–717, https://doi.org/10.1016/0001-6160(85)90035-5.

[31] R.W. Fonda, K.E. Knipling, Texture development in friction stir welds, Sci. Technol. Weld. Join. 16 (2011) 288–294, https://doi.org/10.1179/1362171811Y.0000000010.

[32] R.W. Fonda, J.A. Wert, A.P. Reynolds, W. Tang, Friction stir welding of single crystal aluminium, Sci. Technol. Weld. Join. 12 (2007) 304–310, https://doi.org/10.1179/174329307×197557.

[33] R.W. Fonda, D.J. Rowenhorst, K.E. Knipling, 3D material flow in friction stir welds, Metall. Mater. Trans. A Phys. Metall. Mater. Sci. 50 (2019) 655–663, https://doi.org/10.1007/s11661-018-5021-5.

[34] Y. Zhao, R. Massion, T. Grosdidier, L.S. Toth, Gradient structure in high pressure torsion compacted iron powder, Adv. Eng. Mater. 17 (2015) 1748–1753, https://doi.org/10.1002/adem.201500012.

[35] L.S. Toth, P. Gilormini, J.J. Jonas, Effect of rate sensitivity on the stability of torsion textures, Acta Met. 36 (1988) 3077–3091, https://doi.org/10.1016/0001-6160(88)90045-4.

[36] S.F. Chen, D.Y. Li, S.H. Zhang, H.N. Han, H.W. Lee, M.G. Lee, Modelling continuous dynamic recrystallization of aluminum alloys based on the polycrystal plasticity approach, Int. J. Plast. 131 (2020), https://doi.org/10.1016/j.ijplas.2020.102710.

[37] H.J. Bunge, Texture - the key to physics in polycrystalline matter, Mater. Sci. Forum 273–275 (1998) 3–14, https://doi.org/10.4028/www.scientific.net/msf.273-275.3.

[38] K. Fraser, L.I. Kiss, L. St-Georges, D. Drolet, Optimization of friction stir weld joint quality using a meshfree fully-coupled thermo-mechanics approach, Metals 8 (2018) 101, https://doi.org/10.3390/met8020101.

[39] G.G. Stubblefield, K. Fraser, B.J. Phillips, J.B. Jordon, P.G. Allison, A meshfree computational framework for the numerical simulation of the solid-state additive manufacturing process, additive friction stir-deposition (AFS-D), Mater. Des. 202 (2021), https://doi.org/10.1016/j.matdes.2021.109514.

[40] G.G. Stubblefield, K.A. Fraser, D. Van Iderstine, S. Mujahid, H. Rhee, J.B. Jordon, P.G. Allison, Elucidating the influence of temperature and strain rate on the mechanics of AFS-D through a combined experimental and computational approach, J. Mater. Process. Technol. 305 (2022) 117593, https://doi.org/10.1016/j.jmatprotec.2022.117593.

[41] G.G. Stubblefield, K.A. Fraser, T.W. Robinson, N. Zhu, R.P. Kinser, J.Z. Tew, B.T. Cordle, J.B. Jordon, P.G. Allison, A computational and experimental approach to understanding material flow behavior during additive friction stir deposition (AFSD), Comput. Part. Mech. (2023), https://doi.org/10.1007/s40571-023-00578-x.

[42] N. Gotawala, H.Z. Yu, Material flow path and extreme thermomechanical processing history during additive friction stir deposition, J. Manuf. Process. 101 (2023) 114–127, https://doi.org/10.1016/j.jmapro.2023.05.095.

[43] D.Z. Avery, C.E. Cleek, B.J. Phillips, M.Y. Rekha, R.P. Kinser, H.M. Rao, L.N. Brewer, P.G. Allison, Evaluation of microstructure and mechanical properties of Al-Zn-Mg-Cu alloy repaired via additive friction stir deposition, J. Eng. Mater. Technol. 144 (2022) 1–14, https://doi.org/10.1115/1.4052816.

[44] C. Zeng, H. Ghadimi, H. Ding, S. Nemati, A. Garbie, J. Raush, S. Guo, Microstructure evolution of Al6061 alloy made by additive friction stir deposition, Materials 15 (2022), https://doi.org/10.3390/ma15103676.

[45] R.J. Griffiths, D. Garcia, J. Song, V.K. Vasudevan, M.A. Steiner, W. Cai, H.Z. Yu, Solid-state additive manufacturing of aluminum and copper using additive friction stir deposition: process-microstructure linkages, Materialia 15 (2021) 100967, https://doi.org/10.1016/j.mtla.2020.100967.

[46] B.J. Phillips, C.J.T. Mason, S.C. Beck, D.Z. Avery, K.J. Doherty, P.G. Allison, J.B. Jordon, Effect of parallel deposition path and interface material flow on resulting microstructure and tensile behavior of Al-Mg-Si alloy fabricated by additive friction stir deposition, J. Mater. Process. Technol. 295 (2021) 117169, https://doi.org/10.1016/j.jmatprotec.2021.117169.

[47] S.C. Beck, B.A. Rutherford, D.Z. Avery, B.J. Phillips, H. Rao, M.Y. Rekha, L.N. Brewer, P.G. Allison, J.B. Jordon, The effect of solutionizing and artificial aging on the microstructure and mechanical properties in solid-state additive manufacturing of precipitation hardened Al–Mg–Si alloy, Mater. Sci. Eng. A 819 (2021), https://doi.org/10.1016/j.msea.2021.141351.

[48] C. Ravi, C. Wolverton, First-principles study of crystal structure and stability of Al-Mg-Si-(Cu) precipitates, Acta Mater. 52 (2004) 4213–4227, https://doi.org/10.1016/j.actamat.2004.05.037.

[49] N. Zhu, D.Z. Avery, Y. Chen, K. An, J.B. Jordon, P.G. Allison, L.N. Brewer, Residual stress distributions in AA6061 material produced by additive friction stir deposition, J. Mater. Eng. Perform. 32 (2023) 5535–5544, https://doi.org/10.1007/s11665-022-07483-z.

[50] ALCOA 6061: Extruded Precipitation-Hardenable Aluminum All, Alloy Dig. 55 (2006) Al-281. https://doi.org/10.31399/asm.ad.al0281.

[51] ALUMINUM A206.0: Heat Treatable Aluminum Casting Alloy, Alloy Dig. 32 (1983) Al-244. https://doi.org/10.31399/asm.ad.al0244.

[52] A.A. Coelho, TOPAS and TOPAS-academic: an optimization program integrating computer algebra and crystallographic objects written in C++: An, J. Appl. Crystallogr. 51 (2018) 210–218, https://doi.org/10.1107/S1600576718000183.

[53] R.W. Cheary, A. Coelho, Fundamental parameters approach to x-ray line-profile fitting, J. Appl. Crystallogr. 25 (1992) 109–121, https://doi.org/10.1107/S0021889891010804.

[54] M. Järvinen, Application of symmetrized harmonics expansion to correction of the preferred orientation effect, J. Appl. Crystallogr. 26 (1993) 525–531, https://doi.org/10.1107/S0021889893001219.

[55] P. Scardi, C.L. Azanza Ricardo, C. Perez-Demydenko, A.A. Coelho, Whole powder pattern modelling macros for TOPAS, J. Appl. Crystallogr. 51 (2018) 1752–1765, https://doi.org/10.1107/S160057671801289X.

[56] P. Scardi, M. Ermrich, A. Fitch, E.W. Huang, R. Jardin, R. Kuzel, A. Leineweber, A. Mendoza Cuevas, S.T. Misture, L. Rebuffi, C. Schimpf, Size–strain separation in diffraction line profile analysis, J. Appl. Crystallogr. 51 (2018) 831–843, https://doi.org/10.1107/S1600576718005411.

[57] F. Bachmann, R. Hielscher, H. Schaeben, Texture analysis with MTEX- Free and open source software toolbox, Solid State Phenom. 160 (2010) 63–68, https://doi.org/10.4028/www.scientific.net/SSP.160.63.

[58] R. Hielscher, H. Schaeben, A novel pole figure inversion method: specification of the MTEX algorithm, J. Appl. Crystallogr. 41 (2008) 1024–1037, https://doi.org/10.1107/S0021889808030112.

[59] H.-J. Bunge, Texture Analysis in Materials Science, Elsevier,, 1982, https://doi.org/10.1016/C2013-0-11769-2.

[60] G.E. Dieter. Mechanical Metallurgy, 3rd ed..,, McGraw-Hill,, 2011, https://doi.org/10.5962/bhl.title.35895.

[61] ISO, ISO 13067 - Microbeam analysis. Electron backscatter diffraction, Meas. Aver. grain size 2020 (2020). ⟨https://www.iso.org/standard/74309.html⟩.

[62] F.J. Humphreys, Grain and subgrain characterisation by electron backscatter diffraction, J. Mater. Sci. 36 (2001) 3833–3854, https://doi.org/10.1023/A:1017973432592.

[63] R. Hielscher, H. Schaeben, H. Siemes, Orientation distribution within a single hematite crystal, Math. Geosci. 42 (2010) 359–375, https://doi.org/10.1007/s11004-010-9271-z.

[64] H. Schaeben, A simple standard orientation density function: the hyperspherical de la Valle Poussin kernel, Phys. Status Solidi 200 (1997) 367–376, https://doi.org/10.1002/1521-3951(199704)200:2<367::AID-PSSB367>3.0.CO;2-I.

[65] F. Bachmann, R. Hielscher, H. Schaeben, Grain detection from 2d and 3d EBSD data-Specification of the MTEX algorithm, Ultramicroscopy 111 (2011) 1720–1733, https://doi.org/10.1016/j.ultramic.2011.08.002.

[66] R. Bergmann, R.H. Chan, R. Hielscher, J. Persch, G. Steidl, Restoration of manifold-valued images by half-quadratic minimization, Inverse Probl. Imaging 10 (2016) 281–304, https://doi.org/10.3934/ipi.2016001.

[67] L. Gao, Y. Harada, S. Kumai, Microstructural characterization of aluminum alloys using Weck`s reagent, part I: applications, Mater. Charact. 107 (2014) 426–433, https://doi.org/10.1016/j.matchar.2015.01.005.

[68] L. Gao, Y. Harada, S. Kumai, Microstructural characterization of aluminum alloys using Weck`s reagent, part II: coloring mechanism, Mater. Charact. 107 (2015) 434–452, https://doi.org/10.1016/j.matchar.2015.05.006.

[69] J. Engmann, C. Servais, A.S. Burbidge, Squeeze flow theory and applications to rheometry: a review, J. Nonnewton. Fluid Mech. 132 (2005) 1–27, https://doi.org/10.1016/j.jnnfm.2005.08.007.

[70] S. Mukherjee, A.K. Ghosh, Flow visualization and estimation of strain and strain-rate during friction stir process, Mater. Sci. Eng. A 527 (2010) 5130–5135, https://doi.org/10.1016/j.msea.2010.04.091.

[71] A. Duckham, R.D. Knutsen, O. Engler, Influence of deformation variables on the formation of copper-type shear bands in Al-1Mg, Acta Mater. 49 (2001) 2739–2749, https://doi.org/10.1016/S1359-6454(01)00166-5.

[72] J. Sarkar, Y.V.R.K. Prasad, M.K. Surappa, Optimization of hot workability of an Al-Mg-Si alloy using processing maps, J. Mater. Sci. 30 (1995) 2843–2848, https://doi.org/10.1007/BF00349653.

[73] K. Anderson, J. Weritz, J.G. Kaufman, 6061 and Alclad 6061, Prop. Sel. Alum. Alloy 2 (2019) 388–393, https://doi.org/10.31399/asm.hb.v02b.a0006716.

[74] K.N. Krishnan, On the formation of onion rings in friction stir welds, Mater. Sci. Eng. A. 327 (2002) 246–251, https://doi.org/10.1016/S0921-5093(01)01474-5.

[75] H. Mavridis, G.D. Bruce, G.J. Vancso, G.C. Weatherly, J. Vlachopoulos, Deformation patterns in the compression of polypropylene disks: experiments and simulation, J. Rheol. 36 (1992) 27–43, https://doi.org/10.1122/1.550340.

[76] L.E. Murr, E.A. Trillo, S. Pappu, C. Kennedy, Adiabatic shear bands and examples of their role in severe plastic deformation, J. Mater. Sci. 37 (2002) 3337–3360, https://doi.org/10.1023/A:1016541023502.

[77] T.A. Lychagina, H.G. Brokmeier, Some practical results for calculating elastic properties of textured cubic polycrystals, Phys. Status Solidi Appl. Res. 184 (2001) 373–380, https://doi.org/10.1002/1521-396X(200104)184:2<373::AID-PSSA373>3.0.CO;2-K.

[78] J. Vallin, M. Mongy, K. Salama, O. Beckman, Elastic constants of aluminum, J. Appl. Phys. 35 (1964) 1825–1826, https://doi.org/10.1063/1.1713749.

[79] D. Garcia, W.D. Hartley, H.A. Rauch, R.J. Griffiths, R. Wang, Z.J. Kong, Y. Zhu, H. Z. Yu, In situ investigation into temperature evolution and heat generation during additive friction stir deposition: a comparative study of Cu and Al-Mg-Si, Addit. Manuf. 34 (2020) 101386, https://doi.org/10.1016/j.addma.2020.101386.

[80] P.C. Metz, Z. Arwood, C. Franz, E. Heikkenen, V. Chawla, S.S. Babu, D. Penumadu, K. Page, Non-uniform plastic deformation in additive friction stir deposited Ti-6Al-4V, Materialia 30 (2023) 101799, https://doi.org/10.1016/j.mtla.2023.101799.

[81] N. Saber, B. Leslie G, K. H. Kyungmin, L. Gerald, Z. Congyuan, E. Selami, G. Hamed, G. Shengmin, Z. Yuxuan, B. Hassina, Neutron imaging of Al6061 prepared by solid-state friction stir additive manufacturing, Metals 13 (1) (2022) 11.

[82] P.L. Threadgilll, A.J. Leonard, H.R. Shercliff, P.J. Withers, Friction stir welding of aluminium alloys, Int. Mater. Rev. 54 (2009) 49–93, https://doi.org/10.1179/174328009×411136.

[83] A.A. Khamei, K. Dehghani, R. Mahmudi, Modeling the hot ductility of AA6061 aluminum alloy after severe plastic deformation, Jom 67 (2015) 966–972, https://doi.org/10.1007/s11837-015-1354-3.

[84] B. Derby, The dependence of grain size on stress during dynamic recrystallisation, Acta Metall. Mater. 39 (1991) 955–962, https://doi.org/10.1016/0956-7151(91)90295-C.

[85] P. Scardi, M. Leoni, Whole powder pattern modelling, Acta Crystallogr. Sect. A Found. Crystallogr. 58 (2002) 190–200, https://doi.org/10.1107/S0108767301021298.

[86] N.C. Popa, The (hkl) dependence of diffraction-line broadening caused by strain and size for all laue groups in Rietveld refinement, J. Appl. Crystallogr. 31 (1998) 176–180, https://doi.org/10.1107/S0021889897009795.

[87] T. Adler, C.R. Houska, Simplifications in the x-ray line-shape analysis, J. Appl. Phys. 50 (1979) 3282–3287, https://doi.org/10.1063/1.326368.

[88] P. Scardi, A. Leonardi, L. Gelisio, M.R. Suchomel, B.T. Sneed, M.K. Sheehan, C. K. Tsung, Anisotropic atom displacement in Pd nanocubes resolved by molecular dynamics simulations supported by x-ray diffraction imaging, Phys. Rev. B - Condens. Matter Mater. Phys. 91 (2015) 1–8, https://doi.org/10.1103/PhysRevB.91.155414.

[89] E.J. Mittemeijer, P. Scardi, Diffraction Analysis of the Microstructure of Materials, Springer, Berlin, Heidelberg, 2004, https://doi.org/10.1007/978-3-662-06723-9.

[90] E.J. Mittemeijer, A. Leineweber, U. Welzel, P. Scardi, Fifth size strain conference. Diffraction analysis of the microstructure of materials, OLDENBOURG WISSENSCHAFTSVERLAG,, 2008, https://doi.org/10.1524/9783486992564.

[91] E.J. Mittemeijer, U. Welzel, Modern diffraction, Methods (2013).

[92] F. Crameri, G.E. Shephard, P.J. Heron, The misuse of colour in science communication, Nat. Commun. 11 (2020) 1–10, https://doi.org/10.1038/s41467-020-19160-7.